Image reconstruction from truncated fan-beam projections along a circular trajectory using the virtual fan-beam method

Mathurin Charles, Rolf Clackdoyle, Simon Rit

Image reconstruction from truncated fan-beam projections along a circular trajectory using the virtual fan-beam method

Mathurin Charles[1], Rolf Clackdoyle[1] and Simon Rit[2]

[1] Univ. Grenoble Alpes, CNRS, UMR 5525, VetAgro Sup, Grenoble INP, TIMC, 38000 Grenoble, France

[2] Univ Lyon, INSA-Lyon, Université Claude Bernard Lyon 1, UJM-Saint Etienne, CNRS, Inserm, CREATIS UMR 5220, U1294, F-69373, LYON, France

E-mail: `mathurin.charles@univ-grenoble-alpes.fr`

Abstract. *Objective.* In this paper, we investigate how the virtual fan-beam (VFB) method can be used to perform mathematically correct 2D reconstruction in a region-of-interest (ROI), using truncated fan-beam projections acquired on a circular scan, for truncation that only occurs on one side of the object.

Approach. We start by choosing a virtual fan-beam trajectory and specifying how to obtain the corresponding virtual projections. Then, three VFB formulas are obtained by applying known super-short-scan (SSS) formulas to this virtual trajectory. Two of them perform the backprojection in a virtual parallel geometry and the third in the virtual fan-beam geometry. Next, we develop two VFB formulas that perform the backprojection step in the fan-beam acquisition geometry.

Main results. We present five VFB reconstruction formulas for this truncation setting. To our knowledge, the two VFB formulas performing the backprojection in the fan-beam acquisition geometry are new. Moreover, the five VFB formulas presented here obtain accurate reconstruction in a larger ROI than what has been previously reported in the literature in the same setting. A complete mathematical derivation of these five VFB formulas is given, and their implementation is described step by step. Numerical simulations, using the Forbild head and thorax phantoms, demonstrate the efficacy of these formulas. A spatial resolution analysis and a variance study indicate minor differences between these five VFB formulas.

Significance. This work shows that many different VFB formulas can be applied to perform mathematically correct 2D reconstruction in a ROI, in case of truncated fan-beam projections acquired on a circular scan. Moreover, the two new VFB formulas, with backprojection in the acquisition geometry, may open the path for an extension of the VFB method to 3D reconstruction from transversely truncated cone-beam projection acquired on a circular scan.

1. Introduction

In two-dimensional (2D) computed tomography (CT), the aim is to reconstruct the density function of a 2D object, f, from its projections. Typically, measurements over all lines traversing the object are obtained and grouped either as parallel or fan-beam

projections. In this situation, the well-known filtered backprojection (FBP) algorithm can be applied to reconstruct the object function f (Natterer 1986). To obtain the density $f(\vec{x})$ at any specific point $\vec{x}$ in the plane, the FBP formula uses every line-integral measurement, including those of lines not passing through $\vec{x}$.

In the situation where not every line-integral measurement is available, the approach to image reconstruction, until at least the turn of the century, was to estimate or ignore the missing information prior to reconstruction. Various reconstruction approaches were explored including FBP after estimating the missing measurements (Lewitt 1979, Ohnesorge et al. 2000), iterative schemes based on the known object outline (Ogawa et al. 1984), singular value decomposition (Louis & Rieder 1989), and wavelet approaches (Rashid-Farrokhi et al. 1997).

The most common situation of missing information was and still is truncated projections, where measurements at the edges of some or all of the projections are not available, typically because the object being imaged is too large for the detector. Another case of missing data is a reduced angular range of fan-beam projections where the fan-beam vertex (the x-ray source) follows a circular trajectory but for less than the minimum required to measure all line-integrals through the object. Missing data situations that we do not address here are the interior and exterior problems, and limited-angle data (Natterer 1986).

New understanding emerged shortly after the turn of the century (Clackdoyle & Defrise 2010), establishing the concept of "partial data" rather than "missing data", because the mathematics showed that, in some specific situations, part of the object can be reconstructed ("partial reconstruction") from partial data. The apparent contradiction with the FBP formula, which uses every line-integral for reconstruction of each point of the object, was reconciled by the fact that many different reconstruction formulas exist, as shown by Clackdoyle & Noo (2004) for example.

An early example of partial data reconstruction arose for fan-beam data from a limited angular range (Noo et al. 2002, Chen 2003), later called the "super-short-scan"(SSS) (Kudo et al. 2002). Explicit reconstruction formulas were given for points in the object which were irradiated by x-ray sources from all directions (all 180°), even though other points might not satisfy this condition. This approach has the advantage of being mathematically correct, and can be implemented efficiently. A limitation is the requirement that none of the contributing fan-beam projections can be truncated.

Shortly afterwards, in 2004, another approach appeared which achieved partial reconstruction but from truncated projection data, using a first step of backprojecting the derivative of the projection data. This method has been called differentiated backprojection (DBP) (Noo et al. 2004, Zhuang et al. 2004) or backprojection filtration (BPF) (Zou et al. 2004), and involves a post-backprojection processing using the Hilbert transform. This approach is also mathematically correct. It can handle a broad range of truncated data configurations, and in many cases can be efficiently implemented. However, the line-by-line post-processing of the inverse Hilbert transform can be challenging to implement.

Also in 2004, a different approach to handling truncated projection data appeared, which was based on the SSS fan-beam method even though that method does not allow truncated projections. This approach (Clackdoyle et al. 2004) took the truncated projections and reformulated (or "rebinned") the measurements into new "virtual" fan-beam projections which were not truncated, so the SSS formula (Noo et al. 2002) could then be applied. This approach has since been referred to as the virtual fan-beam (VFB) method, and is the subject of the work presented here. This method also has the advantage of being mathematically correct. A disadvantage is the need to find an appropriate virtual trajectory. Also, this method handles fewer truncated data configurations than the DBP method. However, the VFB approach is complementary to that of DBP because it processes truncated projections in a fundamentally different way (Clackdoyle et al. 2009).

These various analytic approaches provided knowledge as to what partial reconstructions (which regions of the object) can be obtained from specific partial data. Further theoretical understanding and enlarged possibilities arose in 2006 (Defrise et al. 2006) although a general reconstruction formula was not provided. With this information linking measurements to reconstructible regions of the object, iterative reconstruction algorithms (or "discrete-model based" algorithms), such as those described in (Fu et al. 2006, Zhang & Zeng 2007, Rashed et al. 2009, Sidky et al. 2014), produce accurate results. These iterative methods are effective and simple to implement, but suffer the usual difficulties of finding a reliable stopping criteria and of much longer reconstruction times. In a similar category to iterative methods, deep learning approaches are also being applied to partial data problems (Li et al. 2019). These approaches may turn out to be effective but are also "blind" methods that do not provide direct insight into the nature of the reconstruction problem.

Here, we restrict our attention to the particular partial data problem of truncated projections arising from an object that is too large for the detector, and one extremity of it protrudes outside the scanner field-of-view (FOV). As the truncation occurs only from one side of the object, this situation can be seen as a one-sided truncation problem, which we call 'unilateral truncation' in the following. It is not to be confused with the one-sided truncation due to an off-center detector, where only the right or left side of a centered detector is measured (Lux 1981). Although iterative algorithms and the DBP method can be used for this problem, here we are specifically considering the VFB approach, which can reconstruct the same region-of-interest (ROI) as the DBP method for the unilateral truncation considered here (Noo et al. 2004).

The VFB method was first introduced by Clackdoyle et al. (2004), in the context of unilateral truncation. The chosen virtual trajectory was an arc of circle, and the acquisition data were rebinned into the virtual fan-beam geometry before applying a SSS formula to the virtual projections. For more general cases of partial data, Clackdoyle & Noo (2004) described a large class of VFB formulas. These formulas, expressed entirely in the parallel-beam setting, allowed the choice of virtual fan-beam projections to change with each reconstruction point, provided the virtual vertex lay outside a disk

containing the object. For the case of an elliptical object with two extremities protruding outside the FOV ('bilateral truncation'), a VFB procedure was developed by Clackdoyle et al. (2006). This procedure required the area of the object to be less than the area of the FOV. Later, Ould-Mohamed et al. (2007) developed VFB formulas similar to those of Clackdoyle & Noo (2004), but with the flexibility to choose the virtual vertices anywhere outside the smallest convex and compact set supporting the object. These formulas were applied to artificially truncated parallel projections which could not be handled by previous methods (Ould-Mohamed et al. 2008).

For unilateral truncation, the VFB procedure presented by Clackdoyle et al. (2004) applies to a ROI smaller than the maximal ROI for the VFB method (Clackdoyle et al. 2004). For the large class of VFB formulas (Clackdoyle & Noo 2004), the requirement of virtual vertices outside the object disk limits the virtual trajectory and the size of the FOV. The VFB formula developed for bilateral truncation (Clackdoyle et al. 2006) could in principle be applied to unilateral truncation, provided the extended object is not too large compared to the FOV. The formulas of Ould-Mohamed et al. (2007) could be applied to any situation with unilateral truncation, but cannot be applied to fan-beam data without a conversion to parallel-beam geometry.

In this paper, we present five VFB reconstruction formulas customized for fan-beam projections acquired on a full circular trajectory, in case of unilateral truncation and of an object with elliptical support. These five formulas are mathematically correct in the maximal ROI for the VFB method, and differ mainly in which domain is used for the backprojection step. Two of them backproject parallel projections and another performs backprojection in the virtual fan-beam domain. These three formulas correspond to the application of three SSS formulas of Noo et al. (2002) to the virtual fan-beam trajectory. The fourth and fifth formulas, which we believe to be new, perform backprojection in the original acquisition geometry. A first version of these formulas was presented in a conference proceeding by the same authors (Charles et al. 2021), but with one of the formula suffering from a smaller valid reconstruction area compared to the other four. This issue has been resolved in this paper. The numerical simulation section has also been enhanced by using more challenging phantoms and adding a spatial resolution analysis. Furthermore, this paper contains a complete self-contained mathematical derivation of the formulas, and the discretization and implementation of the formulas is described step by step.

The paper is organized as follows: in section 2, we recall the VFB principle, and we present the five reconstruction formulas; in section 3, we specify how the formulas are discretized and implemented; in section 4, we describe the numerical simulations and present the results; in section 5, we discuss these results; finally, in section 6, we draw conclusions.

2. Theory

In this section, we present five VFB-based formulas customized for the setting of fan-beam projections acquired along a full circular trajectory, for an elliptical object with unilateral truncation. Taking advantage of the specificity of this setting, we provide comprehensive demonstrations of these five VFB formulas, including several well-known intermediate results, so that the following mathematical derivations do not rely on other articles.

We begin by recalling the relations linking parallel projections and fan-beam projections acquired along a circular scan. These relations are very well-known, and we provide analytic proofs here. To do so, we introduce two couples, (λ_1, γ_1) and (λ_2, γ_2), which correspond to the parameters of the two fan-beam rays supported by a line intersecting a circular scan (see equations (13) and (14) in section 2.2).

Using this framework, we demonstrate two relations between filtered parallel projections and filtered fan-beam projections, which lead to three SSS formulas for a fan-beam circular acquisition scan, two of them performing parallel backprojection and the third fan-beam backprojection along the circular scan. The proofs we provide for these three formulas, especially for the third one, use a different framework than that of Noo et al. (2002), where their results are derived for the first time.

Next, we recall the principles of the VFB method and apply them to the unilateral truncation setting considered here. Taking advantage of this specific truncation setting, we choose a circular virtual trajectory allowing the reconstruction of the largest possible ROI in this situation for the VFB method. Then, using the fan-beam to parallel projections relations, we derive a rebinning procedure to obtain non-truncated virtual projections from the acquisition data, for any vertex of the circular virtual trajectory chosen. Next, we apply the three SSS formulas derived above to the circular virtual trajectory, resulting in three VFB formulas, two of them using parallel backprojection, and the third fan-beam backprojection in the virtual geometry. These formulas were already known (Clackdoyle et al. 2004), but not customized to obtain the largest possible ROI.

Finally, from the fan-beam to parallel filtered projections relations, we derive a fan-beam to fan-beam filtered projections relation, for two fan-beam circular geometries with different radii, which we believe to be a new result. From this relation, we derive two new VFB formulas, whose novel features are backprojection in the fan-beam acquisition geometry, and directly filtering the non-truncated fan-beam acquisition projections.

2.1. Configuration studied

In the situation we study, fan-beam projections are acquired with a circular source trajectory of radius R_A ('A' stands for acquisition). The FOV, which is the region viewed by every source position, is a disk of radius R_F. The object to be reconstructed has a known elliptic support included inside the disk of radius R_A, but only partially inside the FOV, so most of the fan-beam projections are truncated (see figure 1).

Let $\Lambda_{R_A} = [0, 2\pi)$ denote the angular extent of the acquisition trajectory. We decompose the set of acquisition projections into the sets of non-truncated and truncated projections, of angular extent $\Lambda^C_{R_A}$ and $\Lambda^T_{R_A}$ respectively ('C' and 'T' stand for 'complete' and 'truncated' respectively). So $\{\Lambda^C_{R_A}, \Lambda^T_{R_A}\}$ is a partition of Λ_{R_A}, i.e. we have $\Lambda_{R_A} = \Lambda^C_{R_A} \cup \Lambda^T_{R_A}$ with $\Lambda^C_{R_A} \cap \Lambda^T_{R_A} = \emptyset$. Depending on the supports of the FOV and the object, $\Lambda^C_{R_A}$ is a single interval or the union of two intervals (a configuration illustrating the second case is displayed in figure 1).

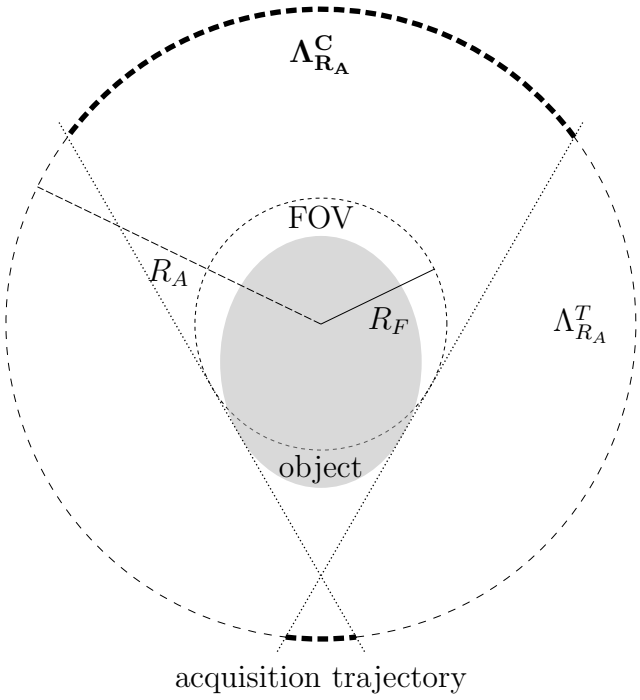

Figure 1. The configuration studied. The acquisition trajectory has a radius R_A and the FOV a radius R_F. The tangents to the object and the FOV delimit the parts of the trajectory for which the projections are non-truncated (bold dashed arcs of circle).

2.2. Notation and relations between parallel and fan-beam geometries

We define the projections in the parallel-beam and fan-beam settings and also the filtered projections that we will use in those two settings. We loosely follow the notation in (Noo et al. 2002). Let f denote the 2D object density to be reconstructed. We assume that the support of f is contained within the interior of the disk of radius R_A (i.e. $f(\vec{x}) = 0$ when $||\vec{x}|| \geq R_A$).

The parallel-beam projections of f are defined by

$$p(\phi, s) = \int_{\mathbb{R}} f(l\vec{\theta}_\phi + s\vec{\eta}_\phi)\mathrm{d}l, \ \phi \in [0, 2\pi), \ s \in (-R_A, R_A), \tag{1}$$

where $\vec{\theta}_\phi = (\cos\phi, \sin\phi)$ and $\vec{\eta}_\phi = (-\sin\phi, \cos\phi)$. In the following, as $\phi \mapsto p(\phi, s)$ is 2π-periodic, if the first parameter of p is outside $[0, 2\pi)$ then we implicitly consider its

value modulo 2π. From equation (1), it is easy to verify that

$$p(\phi, s) = p(\phi + \pi, -s), \tag{2}$$

which shows that there are two possible parallel parametrizations for a given line-integral. Let $h_F(s) = \int_{\mathbb{R}} |\sigma| e^{2\mathrm{i}\pi\sigma s} \mathrm{d}\sigma$ (formally) denote the ramp filter. The ramp-filtered parallel projections are defined by

$$p_F(\phi, s) = \int_{\mathbb{R}} h_F(s - s') p(\phi, s') \mathrm{d}s'. \tag{3}$$

From equations (2) and (3) and the fact that $h_F(-s) = h_F(s)$, it follows that

$$p_F(\phi, s) = p_F(\phi + \pi, -s). \tag{4}$$

Let $h_H(s) = \int_{\mathbb{R}} -\mathrm{i}\ \mathrm{sign}(\sigma) \mathrm{e}^{2\mathrm{i}\pi\sigma s} \mathrm{d}\sigma$ (formally) denote the Hilbert filter. The Hilbert-filtered parallel projections are defined by

$$p_H(\phi, s) = \int_{\mathbb{R}} h_H(s - s') p(\phi, s') \mathrm{d}s'. \tag{5}$$

Similarly, from equations (2) and (5) and the fact that $h_H(-s) = -h_H(s)$, we obtain

$$p_H(\phi, s) = -p_H(\phi + \pi, -s). \tag{6}$$

Moreover, $(\partial/\partial s) h_H(s) = \int_{\mathbb{R}} -\mathrm{i}\ \mathrm{sign}(\sigma)(2\mathrm{i}\pi\sigma) e^{2\mathrm{i}\pi\sigma s} \mathrm{d}\sigma = 2\pi h_F(s)$ (see Deans (1983, p. 139, remark 1)) so it follows, and is well-known (e.g. (Noo et al. 2002)), that

$$p_F(\phi, s) = \frac{1}{2\pi} \frac{\partial}{\partial s} p_H(\phi, s). \tag{7}$$

Using p_F, defined in equation (3), image reconstruction can be performed with the well-known parallel FBP formula (see (Kak & Slaney 1988) for instance):

$$f(\vec{x}) = \int_0^{\pi} \left[p_F(\phi, s) \right]\big|_{s = \vec{x} \cdot \vec{\eta}_\phi} \mathrm{d}\phi. \tag{8}$$

The fan-beam projections of f for a circular source trajectory of radius R are defined by

$$g^R(\lambda, \gamma) = \int_0^{\infty} f(R\vec{\theta}_\lambda + t\vec{\theta}_{\lambda+\pi+\gamma}) \mathrm{d}t,\ \lambda \in [0, 2\pi),\ \gamma \in (-\pi, \pi). \tag{9}$$

Here, λ indicates the angular position of the source, and γ is the ray-angle, measured from the central ray, which goes from the source to the center of rotation. Unlike (Noo et al. 2002), we choose to measure γ counterclockwise, also. For circular fan-beam geometries, these are typical parameters, see e.g. (Kak & Slaney 1988). In the following, as $\lambda \mapsto g^R(\lambda, \gamma)$ is 2π-periodic, if the first parameter of g^R is outside $[0, 2\pi)$, then we implicitly consider its value modulo 2π, and similarly for the second parameter, γ. The Hilbert-filtered fan-beam projections are defined by (Noo et al. 2002, eq. (13))

$$g_H^R(\lambda, \gamma) = \int_{-\pi}^{\pi} h_H(\sin(\gamma - \gamma'))\ g^R(\lambda, \gamma') \mathrm{d}\gamma' \tag{10}$$

and we introduce a second type of filtered fan-beam projections, defined by (Noo et al. 2002, eq. (34))

$$g_F^R(\lambda, \gamma) = \frac{1}{2\pi} \int_{-\pi}^{\pi} h_H(\sin(\gamma - \gamma')) \left(\frac{\partial}{\partial \lambda} - \frac{\partial}{\partial \gamma'} \right) g^R(\lambda, \gamma') \mathrm{d}\gamma', \tag{11}$$

which satisfies the following property:

$$g_F^R(\lambda,\gamma) = \frac{1}{2\pi}\left(\frac{\partial}{\partial\lambda} - \frac{\partial}{\partial\gamma}\right) g_H^R(\lambda,\gamma). \tag{12}$$

To demonstrate this property, we rewrite g_H^R as $g_H^R(\lambda,\gamma) = \int_{-\pi}^{\pi} h_H(\sin\gamma')\, g^R(\lambda,\gamma-\gamma')\mathrm{d}\gamma'$ and inject this expression in (12) to obtain (11).

We can now link fan-beam and parallel projections. Given $\phi \in [0, 2\pi)$ and $s \in (-R_A, R_A)$, we define (λ_1, γ_1) and (λ_2, γ_2) as follows:

$$\lambda_1(\phi,s) = \phi + \pi - \arcsin(s/R_A), \qquad \gamma_1(s) = \arcsin(s/R_A), \tag{13a}$$

$$\lambda_2(\phi,s) = \phi + \arcsin(s/R_A), \qquad \gamma_2(s) = -\arcsin(s/R_A), \tag{13b}$$

so $\gamma_1, \gamma_2 \in (-\pi/2, \pi/2)$. Note that λ_1, γ_1 and λ_2, γ_2 are expressions in (ϕ, s) and not independent variables. We will now show that

$$p(\phi,s) = g^{R_A}(\lambda_1,\gamma_1), \tag{14a}$$

$$= g^{R_A}(\lambda_2,\gamma_2). \tag{14b}$$

Geometrically, these relations correspond to the configurations displayed in figure 2.

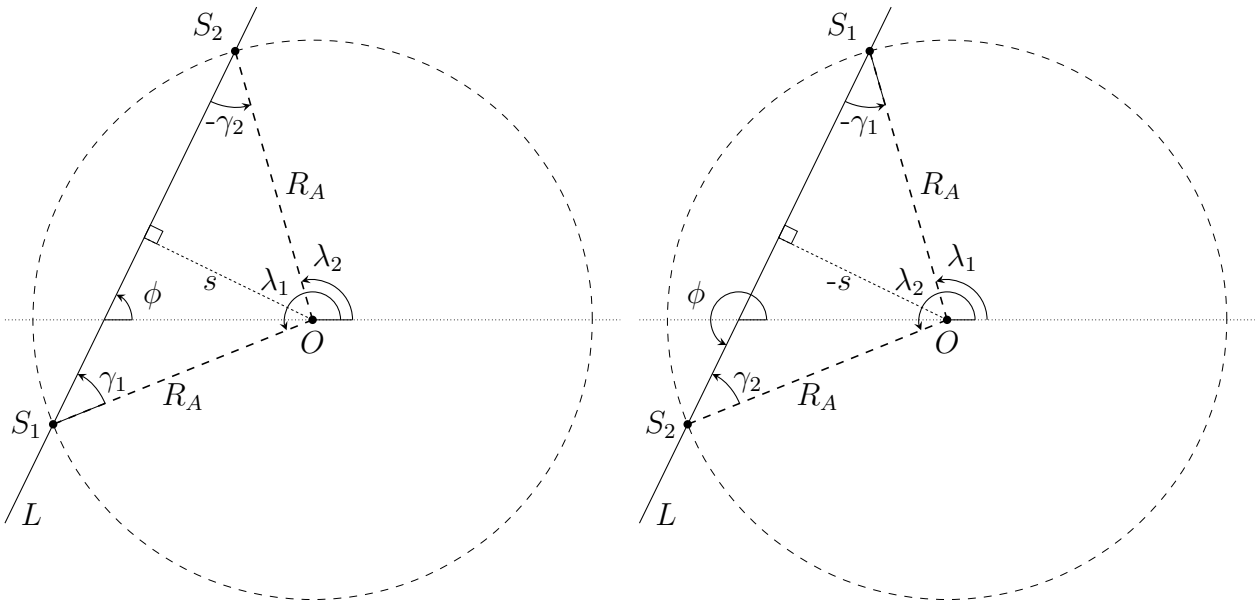

Figure 2. The line L of parallel parameters (ϕ, s) intersects the circle C of radius R_A at S_1 and S_2. The fan-beam rays (half-lines) emitted from S_1 and S_2 along L and inside C are defined by the parameters (λ_1, γ_1) and (λ_2, γ_2) respectively. The two possible cases are shown (left: $s > 0$, right: $s < 0$). All angles are measured counterclockwise.

For an analytic demonstration of (14a) and (14b), we first have to establish that the integration limits in equation (9), for $R = R_A$ and $\gamma \in (-\pi/2, \pi/2)$, can be extended from (0,∞) to (-∞,∞), so that they match those of equation (1). For $\vec{x} = R_A\vec{\theta}_\lambda + t\vec{\theta}_{\lambda+\pi+\gamma}$, we obtain $\vec{x}\cdot\vec{\theta}_\lambda = R_A - t\cos(\gamma) \geq R_A$ for $t \leq 0$ and

$\gamma \in (-\pi/2, \pi/2)$ so $||\vec{x}|| \geq |\vec{x} \cdot \vec{\theta}_\lambda| \geq R_A$. Since $f(\vec{x}) = 0$ when $||\vec{x}|| \geq R_A$, we have $\int_{-\infty}^{0} f(R_A\vec{\theta}_\lambda + t\vec{\theta}_{\lambda+\pi+\gamma})\mathrm{d}t = 0$, so for all $\gamma \in (-\pi/2, \pi/2)$, we obtain

$$g^{R_A}(\lambda, \gamma) = \int_{\mathbb{R}} f(R_A\vec{\theta}_\lambda + t\vec{\theta}_{\lambda+\pi+\gamma})\mathrm{d}t. \tag{15}$$

Then, for given $(\phi, s) \in [0, 2\pi) \times (-R_A, R_A)$, we start with (15), and use the definitions of λ_1 and γ_1 to evaluate $g^{R_A}(\lambda_1, \gamma_1) = \int_{\mathbb{R}} f(R_A\vec{\theta}_{\lambda_1} + t\vec{\theta}_{\lambda_1+\pi+\gamma_1})\mathrm{d}t = \int_{\mathbb{R}} f(R_A\vec{\theta}_{\phi+\pi-\gamma_1} + t\vec{\theta}_\phi)\mathrm{d}t$. We first change integration variable $t = R_A\cos\gamma_1 + l$, and then apply $\vec{\theta}_{\phi+\tau} - \cos\tau\ \vec{\theta}_\phi = \sin\tau\ \vec{\eta}_\phi$ with $\tau = -\gamma_1$, to yield

$$\begin{aligned} g^{R_A}(\lambda_1, \gamma_1) &= \int_{\mathbb{R}} f(R_A(-\vec{\theta}_{\phi-\gamma_1} + \cos\gamma_1\vec{\theta}_\phi) + l\vec{\theta}_\phi)\mathrm{d}l \\ &= \int_{\mathbb{R}} f(R_A(-\sin(-\gamma_1)\vec{\eta}_\phi) + l\vec{\theta}_\phi)\mathrm{d}l \\ &= \int_{\mathbb{R}} f(s\vec{\eta}_\phi + l\vec{\theta}_\phi)\mathrm{d}l = p(\phi, s) \end{aligned} \tag{16}$$

which establishes (14a). For (14b), a similar proof applies, but with the change of variables $t = R_A\cos\gamma_2 - l$. Alternatively, we can use (2), $p(\phi, s) = p(\phi + \pi, -s)$: we established that $p(\phi, s) = g^{R_A}(\lambda_1(\phi, s), \gamma_1(s))$ so $p(\phi + \pi, -s) = g^{R_A}(\lambda_1(\phi + \pi, -s), \gamma_1(-s))$. From the definitions of λ_1, λ_2 we note that $\lambda_1(\phi + \pi, -s) = (\phi + \pi) + \pi - \arcsin(-s/R_A) = \phi + \arcsin(s/R_A) + 2\pi = \lambda_2(\phi, s) + 2\pi$ and $\gamma_1(-s) = \gamma_2(s)$. Therefore $p(\phi, s) = p(\phi + \pi, -s) = g^{R_A}(\lambda_2, \gamma_2)$ which establishes (14b).

We will need the reverse relationship for the more general case of a virtual circular trajectory, where the support of f is not necessarily contained within the disk of radius R_V. Specifically, given (λ, γ), what are the values of $(\phi_{\lambda,\gamma}, s_{\lambda,\gamma})$ such that $g^{R_V}(\lambda, \gamma) = p(\phi_{\lambda,\gamma}, s_{\lambda,\gamma})$? Again, under the assumption that the half-line-integral $g^{R_V}(\lambda, \gamma)$ is equal to the line-integral, i.e. $g^{R_V}(\lambda, \gamma) = \int_{\mathbb{R}} f(R_V\vec{\theta}_\lambda + t\vec{\theta}_{\lambda+\pi+\gamma})\mathrm{d}t$, the following rebinning relationship is well-known (for example, (Kak & Slaney 1988, Guerrero et al. 2023)):

$$g^{R_V}(\lambda, \gamma) = p(\lambda + \gamma, -R_V\sin\gamma). \tag{17}$$

We provide the analytic demonstration. Starting from the left-hand side, changing variables $t = R_V\cos\gamma - l$ and again using the relation $\vec{\theta}_{A+B} - \cos B\ \vec{\theta}_A = \sin B\vec{\eta}_A$ with $A = \lambda + \gamma$, $B = -\gamma$, we obtain

$$\begin{aligned} g^{R_V}(\lambda, \gamma) &= \int_{\mathbb{R}} f(R_V\vec{\theta}_\lambda + (R_V\cos\gamma - l)\vec{\theta}_{\lambda+\pi+\gamma})\mathrm{d}l \\ &= \int_{\mathbb{R}} f(R_V\vec{\theta}_{\lambda+\gamma-\gamma} + (l - R_V\cos\gamma)\vec{\theta}_{\lambda+\gamma})\mathrm{d}l \\ &= \int_{\mathbb{R}} f(R_V(\vec{\theta}_{\lambda+\gamma-\gamma} - \cos(-\gamma)\vec{\theta}_{\lambda+\gamma}) + l\vec{\theta}_{\lambda+\gamma})\mathrm{d}l \\ &= \int_{\mathbb{R}} f(R_V\sin(-\gamma)\vec{\eta}_{\lambda+\gamma} + l\vec{\theta}_{\lambda+\gamma})\mathrm{d}l \\ &= p(\lambda + \gamma, -R_V\sin\gamma) \end{aligned} \tag{18}$$

as claimed.

2.3. The super-short-scan method

We now recall the main results of the SSS method (Noo et al. 2002) as applied to the special case of a circular source trajectory or a circular arc source trajectory composed of non-truncated fan-beam projections. These results will be used later in the VFB method. In this section, to emphasize that we consider any fan-beam trajectory, we use a radius R instead of R_A, so the previous definitions made with R_A such as those of (λ_i, γ_i) will be considered here with R. Λ_R will denote the angular extent of the fan-beam trajectory of radius R, whose projections g^R are all non-truncated. More precisely, Λ_R will be an interval or union of intervals, such that $\Lambda_R \subset [0, 2\pi)$.

The support of f is no longer required to be within the disk of radius R, but any point to be reconstructed has to satisfy this condition. The main result is that p_H and p_F can be expressed respectively in terms of g_H^R and g_F^R for any line intersecting the fan-beam trajectory. Consequently, if all lines passing through a point $\vec{x}$ intersect the fan-beam trajectory, then we can compute the parallel filtered projections corresponding to these lines and apply the parallel FBP (8) to reconstruct $f(\vec{x})$. Moreover, we will see that it is possible to backproject directly along the fan-beam trajectory to compute any $f(\vec{x})$ for $\vec{x}$ satisfying the condition above.

The fundamental result on which the SSS method is based, sometimes called the Hilbert projection equality (Clackdoyle & Defrise 2010), was first presented by Hamaker et al. (1980), and later by Noo et al. (2002) for the specific 2D context. With our notation, it is written

$$p_H(\phi, s) = g_H^R(\lambda_1, \gamma_1) \tag{19a}$$

and

$$p_H(\phi, s) = -g_H^R(\lambda_2, \gamma_2). \tag{19b}$$

To show (19a) and (19b) we use the identity $\sin(A - B) = -\vec{\eta}_A \cdot \vec{\theta}_B$ with $A = \phi$ and $B = \phi + \gamma - \gamma_1$. Recalling the rebinning formulas for λ_1 and γ_1, (13a), for given (ϕ, s) we have

$$\begin{aligned} g_H^R(\lambda_1, \gamma_1) &= \int_{-\pi}^{\pi} h_H(\sin(\gamma_1 - \gamma))\ g^R(\lambda_1, \gamma) \mathrm{d}\gamma \\ &= \int_{-\pi}^{\pi} h_H(-\vec{\eta}_\phi \cdot \vec{\theta}_{\phi+\gamma-\gamma_1}) \int_0^{\infty} f(R\vec{\theta}_{\lambda_1} + t\vec{\theta}_{\lambda_1+\pi+\gamma}) \mathrm{d}t\mathrm{d}\gamma \\ &= \int_{-\pi}^{\pi} \int_0^{\infty} t\ h_H(-\vec{\eta}_\phi \cdot t\vec{\theta}_{\phi+\gamma-\gamma_1}) f(R\vec{\theta}_{\phi+\pi-\gamma_1} + t\vec{\theta}_{\phi+\gamma-\gamma_1}) \mathrm{d}t\mathrm{d}\gamma \end{aligned}$$

where the degree -1 homogeneity of h_H was applied. We now perform the polar to rectangular change of variables $\vec{x} = R\vec{\theta}_{\phi+\pi-\gamma_1} + t\vec{\theta}_{\phi+\gamma-\gamma_1}$, so $t\mathrm{d}t\mathrm{d}\gamma = \mathrm{d}\vec{x}$.

$$\begin{aligned} g_H^R(\lambda_1, \gamma_1) &= \int_{-\infty}^{\infty} \int_{-\infty}^{\infty} h_H(-\vec{\eta}_\phi \cdot (\vec{x} - R\vec{\theta}_{\phi+\pi-\gamma_1})) f(\vec{x}) \mathrm{d}\vec{x} \\ &= \int_{-\infty}^{\infty} \int_{-\infty}^{\infty} h_H(R\sin\gamma_1 - \vec{\eta}_\phi \cdot \vec{x}) f(\vec{x}) \mathrm{d}\vec{x} \end{aligned}$$

$$= \int_{-\infty}^{\infty}\int_{-\infty}^{\infty} h_H(s-\vec{\eta}_\phi\cdot\vec{x})f(\vec{x})\mathrm{d}\vec{x}$$
$$= \int_{-\infty}^{\infty}\int_{-\infty}^{\infty} h_H(s-s')f(l\vec{\theta}_\phi+s'\vec{\eta}_\phi)\mathrm{d}l\mathrm{d}s'$$
$$= \int_{-\infty}^{\infty} h_H(s-s')p(\phi,s')\mathrm{d}s' = p_H(\phi,s) \qquad (20)$$

where the last change of variables was $\vec{x} = l\vec{\theta}_\phi + s'\vec{\eta}_\phi$ with $\mathrm{d}\vec{x} = \mathrm{d}l\mathrm{d}s'$. The proof of (19$b$), $g_H^R(\lambda_2,\gamma_2) = -p_H(\phi,s)$, follows very similar lines. Alternatively, we can use equation (6) with equation (19a). Applying the definitions of λ_1,γ_1 and λ_2,γ_2, we obtain $p_H(\phi,s) = -p_H(\phi+\pi,-s) = -g_H^R(\lambda_1(\phi+\pi,-s),\gamma_1(-s)) = -g_H^R(\lambda_2(\phi,s),\gamma_2(s))$, and thus $p_H(\phi,s) = -g_H^R(\lambda_2,\gamma_2)$, which establishes (19$b$).

Similarly, p_F can be expressed from g_F^R by

$$p_F(\phi,s) = -\frac{1}{\sqrt{R^2-s^2}}g_F^R(\lambda_1,\gamma_1) \qquad (21a)$$

and

$$p_F(\phi,s) = -\frac{1}{\sqrt{R^2-s^2}}g_F^R(\lambda_2,\gamma_2). \qquad (21b)$$

From the definitions $\lambda_1(\phi,s) = \phi+\pi-\arcsin(s/R)$ and $\gamma_1(s) = \arcsin(s/R)$, and the identity $(\partial/\partial u)\arcsin(u) = 1/\sqrt{1-u^2}$, we see that $\partial\lambda_1(\phi,s)/\partial s = -1/\sqrt{R^2-s^2} = -\partial\gamma_1(s)/\partial s$. Using the notation $\partial_i g_H^R$ to denote the partial derivative of g_H^R with respect to the i-th variable, we have from equations (7), (19a) and (12)

$$p_F(\phi,s) = \frac{1}{2\pi}\frac{\partial}{\partial s}p_H(\phi,s) = \frac{1}{2\pi}\frac{\partial}{\partial s}g_H^R(\lambda_1(\phi,s),\gamma_1(s))$$
$$= -\frac{1}{2\pi\sqrt{R^2-s^2}}(\partial_1 g_H^R(\lambda_1,\gamma_1) - \partial_2 g_H^R(\lambda_1,\gamma_1))$$
$$= -\frac{1}{\sqrt{R^2-s^2}}g_F^R(\lambda_1,\gamma_1) \qquad (22)$$

which establishes equation (21a). Equation (21b) follows similarly, since $\partial\lambda_2/\partial s = 1/\sqrt{R^2-s^2} = -\partial\gamma_2/\partial s$.

A well-known fan-beam version of (2) is $g^R(\lambda,\gamma) = g^R(\lambda+\pi+2\gamma,-\gamma)$. We will need a similar version for filtered projections g_F^R. From equations (21a) and (21b), we can show that, for all $\lambda\in[0,2\pi)$ and $\gamma\in(-\pi/2,\pi/2)$,

$$g_F^R(\lambda,\gamma) = g_F^R(\lambda+\pi+2\gamma,-\gamma). \qquad (23)$$

Combining (21a) and (21b), we obtain $g_F^R(\lambda_1,\gamma_1) = -\sqrt{R^2-s^2}p_F(\phi,s) = g_F^R(\lambda_2,\gamma_2)$. Then, using (13) for any (ϕ,s), we have $\lambda_2+\pi+2\gamma_2 = \lambda_1$ and $-\gamma_2 = \gamma_1$. Therefore, $g_F^R(\lambda_2+\pi+2\gamma_2,-\gamma_2) = g_F^R(\lambda_1,\gamma_1) = g_F^R(\lambda_2,\gamma_2)$. Now, given any $(\lambda,\gamma)\in[0,2\pi)\times(-\pi/2,\pi/2)$, we choose $s(\gamma) = -R\sin\gamma$ and $\phi(\lambda,\gamma) = \lambda+\gamma$, and obtain $\lambda_2(\phi(\lambda,\gamma),s(\gamma)) = \lambda$ and $\gamma_2(s(\gamma)) = \gamma$. This choice of (ϕ,s) applied to $g_F^R(\lambda_2,\gamma_2) = g_F^R(\lambda_2+\pi+2\gamma_2,-\gamma_2)$ establishes (23).

From relations (19) and (21), two SSS formulas can be established. They are both based on the parallel FBP formula (8) and differ on how to obtain the filtered parallel

projections p_F. The first SSS formula computes g_H with (10), then obtain p_H from g_H with (19), and finally converts p_H to p_F with (7), before applying formula (8). The second SSS formula computes g_F with (11), and directly obtain p_F from g_F with (21), before applying (8). To reconstruct $f(\vec{x})$, these SSS formulas require p_F or p_H to be known on the set of parallel lines parameterized by $(\phi, \vec{x} \cdot \vec{\eta}_\phi)$ for all $\phi \in [0, 2\pi)$, which amounts to the set of lines passing through $\vec{x}$. Using the rebinning relations (19) and (21) between fan-beam and parallel geometries, p_H and p_F are available for all lines intersecting the fan-beam trajectory. So both SSS formulas provide reconstruction of a point $\vec{x}$ only if all lines through $\vec{x}$ intersect the fan-beam trajectory.

Finally, as shown by Noo et al. (2002), instead of rebinning the filtered fan-beam projections into filtered parallel projections to perform parallel backprojection, it is possible to directly perform the backprojection in the fan-beam acquisition geometry. To that end, a non-negative fan-beam weighting function $w^R(\lambda, \gamma)$ is introduced which must satisfy the following property.

$$w^R(\lambda_1, \gamma_1) + w^R(\lambda_2, \gamma_2) = 1 \text{ for all } \phi \in [0, \pi), s \in (-R, R), \tag{24}$$

recalling that $\lambda_1, \lambda_2, \gamma_1, \gamma_2$ are all expressions in (ϕ, s). Conceptually, each ray is available from two different fan-beam projections, and a weight is assigned to each, such that the total summed weight for the ray is one. (Similarly to g_F, we implicitly take the first variable of w^R to be modulo 2π.) The purpose of the weighting function w^R will become clear below, but for now we note that setting $w^R(\lambda, \gamma) = 1/2$ (for all $(\lambda, \gamma) \in [0, 2\pi) \times (-\pi/2, \pi/2)$) will satisfy the normalization requirement (24). To obtain a suitable fan-beam FBP formula, the basic idea is to replace p_F by g_F^R in the parallel FBP formula (8), using $(21a)$ and $(21b)$. We assume that $||\vec{x}|| < R$. We have

$$\begin{aligned}
f(\vec{x}) &= \int_0^\pi \left[p_F(\phi, s)\right]\big|_{s=\vec{x}\cdot\vec{\eta}_\phi} \mathrm{d}\phi \\
&= \int_0^\pi \left[\left(w^R(\lambda_1, \gamma_1) + w^R(\lambda_2, \gamma_2)\right) p_F(\phi, s)\right]\big|_{s=\vec{x}\cdot\vec{\eta}_\phi} \mathrm{d}\phi \\
&= \int_0^\pi \left[w^R(\lambda_1, \gamma_1) \left(\frac{-1}{\sqrt{R^2 - s^2}}\right) g_F^R(\lambda_1, \gamma_1)\right]\Bigg|_{s=\vec{x}\cdot\vec{\eta}_\phi} \mathrm{d}\phi \\
&\quad + \int_0^\pi \left[w^R(\lambda_2, \gamma_2) \left(\frac{-1}{\sqrt{R^2 - s^2}}\right) g_F^R(\lambda_2, \gamma_2)\right]\Bigg|_{s=\vec{x}\cdot\vec{\eta}_\phi} \mathrm{d}\phi.
\end{aligned} \tag{25}$$

We show in Appendix A that the first term $f_1(\vec{x})$ and the second term $f_2(\vec{x})$ of (25) can be written

$$f_1(\vec{x}) = -\int_{\Lambda_1(\vec{x})} \frac{1}{||\vec{x} - R\vec{\theta}_\lambda||} \left[w^R(\lambda, \gamma) g_F^R(\lambda, \gamma)\right]\big|_{\gamma=\gamma^R_{\vec{x},\lambda}} \mathrm{d}\lambda \tag{26}$$

and

$$f_2(\vec{x}) = -\int_{\Lambda_2(\vec{x})} \frac{1}{||\vec{x} - R\vec{\theta}_\lambda||} \left[w^R(\lambda, \gamma) g_F^R(\lambda, \gamma)\right]\big|_{\gamma=\gamma^R_{\vec{x},\lambda}} \mathrm{d}\lambda \tag{27}$$

where, for $\vec{x} = (x_1, x_2)$,

$$\Lambda_1(\vec{x}) = [\pi - \arcsin(x_2/R), 2\pi + \arcsin(x_2/R)), \tag{28}$$

$$\Lambda_2(\vec{x}) = [\arcsin(x_2/R), \pi - \arcsin(x_2/R)), \tag{29}$$

and

$$\gamma^R_{\vec{x},\lambda} = -\arcsin\left(\frac{\vec{x}\cdot\vec{\eta}_\lambda}{||\vec{x} - R\vec{\theta}_\lambda||}\right). \tag{30}$$

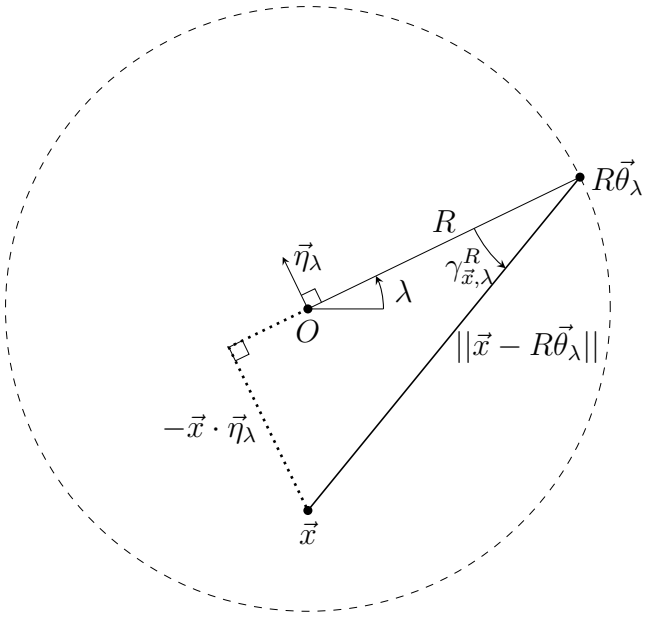

Figure 3. View of the angle $\gamma^R_{\vec{x},\lambda} = -\arcsin(\vec{x}\cdot\vec{\eta}_\lambda/||\vec{x} - R\vec{\theta}_\lambda||)$ between the central ray (passing through O) and the ray passing through $\vec{x}$.

A geometrical illustration of $\gamma^R_{\vec{x},\lambda}$ is given in figure 3. The expressions for the integrands of $f_1(\vec{x})$ and $f_2(\vec{x})$ are the same, and the integration ranges $\Lambda_1(\vec{x})$ and $\Lambda_2(\vec{x})$ are contiguous intervals with no overlap. Therefore, from (25),

$$f(\vec{x}) = f_1(\vec{x}) + f_2(\vec{x}) = -\int_{\Lambda_1(\vec{x})\cup\Lambda_2(\vec{x})} \frac{1}{||\vec{x} - R\vec{\theta}_\lambda||} \left[w^R(\lambda,\gamma) g^R_F(\lambda,\gamma)\right]\Big|_{\gamma=\gamma^R_{\vec{x},\lambda}} \mathrm{d}\lambda. \tag{31}$$

Because $\Lambda_2(\vec{x}) \cup \Lambda_1(\vec{x}) = [\arcsin(x_2/R), 2\pi + \arcsin(x_2/R))$, and since the integrand is periodic (in λ) of period 2π, we can shift the integration limits by the constant quantity $\arcsin(x_2/R)$ and write, for our final fan-beam FBP result,

$$f(\vec{x}) = -\int_0^{2\pi} \frac{1}{||\vec{x} - R\vec{\theta}_\lambda||} \left[w^R(\lambda,\gamma) g^R_F(\lambda,\gamma)\right]\Big|_{\gamma=\gamma^R_{\vec{x},\lambda}} \mathrm{d}\lambda, \tag{32}$$

which corresponds to (33) in (Noo et al. 2002).

We now discuss the role of the weight w^R. As shown by (21a) and (21b), the filtered data $g^R_F(\lambda_1,\gamma_1)$ and $g^R_F(\lambda_2,\gamma_2)$ are redundant. Condition (24) ensures that the total weight attributed to these redundant data is always one (see (25)). As mentioned earlier, setting $w^R(\lambda,\gamma) = 1/2$ satisfies (24). However, this uniform weighting is only possible if all the filtered data are available, i.e. for a full-scan.

For a partial scan $\Lambda_R \subsetneq [0, 2\pi)$, some projections are missing, so some filtered projections are not available. In that case, w^R provides an essential mechanism to

compensate with the redundant data. If only one of the two filtered projection values $g_F^R(\lambda_i, \gamma_i)$ for $i \in \{1, 2\}$ is available, we have to attribute all the weight (i.e. a weight of one) to the available one while assigning a zero weight to the unavailable one (so that unavailable data are not used).

For a fan-beam ray of parameters (λ, γ), the redundant filtered data are $g_F^R(\lambda, \gamma)$ and $g_F^R(\lambda + \pi + 2\gamma, -\gamma)$, as shown by (23). So for a fan-beam trajectory of angular extent Λ_R composed of non-truncated projections, we can define the redundancy weight w^R on $[0, 2\pi) \times (-\pi/2, \pi/2)$ by:

$$w^R(\lambda, \gamma) = \begin{cases} \frac{1}{2} & \text{if} \quad \lambda \in \Lambda_R \text{ and } \lambda + \pi + 2\gamma \in \Lambda_R, \\ 1 & \text{if} \quad \lambda \in \Lambda_R \text{ and } \lambda + \pi + 2\gamma \notin \Lambda_R, \\ 0 & \text{if} \quad \lambda \notin \Lambda_R, \end{cases} \tag{33}$$

where $\lambda + \pi + 2\gamma$ is considered modulo 2π. We note that for a line with parameters (ϕ, s) not intersecting the source trajectory, both weights $w^R(\lambda_1(\phi, s), \gamma_1(s))$ and $w^R(\lambda_2(\phi, s), \gamma_2(s))$ are zero, so (24) is not satisfied. Therefore, formula (32) cannot be applied to reconstruct points $\vec{x}$ for which there are lines through $\vec{x}$ not intersecting the source trajectory.

2.4. Principles of the virtual fan-beam method

To use the SSS formulas of Noo et al. (2002), a key step is the computation of either g_H^R or g_F^R. However, equations (10) and (11) require non-truncated fan-beam projections, so it is not possible to directly compute $g_H^{R_A}$ or $g_F^{R_A}$ in case of truncation. The idea of the VFB method is to look for a virtual trajectory for which we have non-truncated projections and to rebin the data into this virtual geometry. Following the SSS theory, image reconstruction can be obtained for each point of the object for which all lines passing through this point intersect the virtual trajectory.

The choice of the virtual trajectory is constrained by the requirement of non-truncation of the virtual fan-beam projections: for any virtual source point, measurements must be available for all half-lines from this point passing through the object. Although virtual source points inside the object are possible in theory, in practice it is not possible to obtain half-line data from such locations. Now, because the acquisition trajectory is a full circle, all line-integrals passing through the FOV are known so points inside the FOV are good potential candidates for virtual source points. For any such point inside the FOV, the goal is to obtain half-line-integrals from line-integrals. This is possible only if, in any direction, one of the two half-line-integrals is zero so that the other is equal to the line-integral. This condition is ensured for any point outside the convex hull of the object. Thus any point in the FOV and outside the convex hull of the object can be chosen as a virtual source point. If we choose a circular virtual trajectory, then its radius has to be less or equal than R_F to stay in the FOV. Although other choices are also possible, we take as virtual trajectory the circular arc of radius $R_V = R_F$ that lies outside the convex hull of the object.

2.5. Detailed rebinning procedure

We now describe how the rebinning from the acquisition geometry of radius R_A to the virtual trajectory of radius R_V can be performed.

First, the virtual trajectory is restricted to the points $R_V\vec{\theta}_\lambda$ that are outside the convex hull of the object. We define Λ_{R_V}, the angular extent of the virtual trajectory, by $\Lambda_{R_V} = \{\lambda \in [0, 2\pi) | R_V\vec{\theta}_\lambda \text{ is outside the convex hull of the object}\}$.

Then, for any virtual source point, we have to determine, in any direction, to which of the two half-lines we attribute the line-integral. There are two possibilities. First, the line does not intersect the object. In that case the line-integral and both half-line-integrals are zero, so we can attribute the zero line-integral to either one of the two half-lines. Second, the line intersects the object. Since the virtual source point is outside the convex hull of the object, only one of the two half-lines intersect the object so we assign the line-integral to this half-line. We note therefore that at most half of the half-lines from a virtual source intersect the object, and furthermore they form a single continuous range of angles. In terms of the angular parameter γ of g^{R_V}, it means that the half-lines intersecting the object belong to an interval in γ of length π at most. This γ-interval can be expressed as $\Gamma(s^{R_V}(\lambda)) = [-\pi/2 + s^{R_V}(\lambda), \pi/2 + s^{R_V}(\lambda))$ where s^{R_V} is an offset angle depending on the virtual source position $R_V\vec{\theta}_\lambda$ and on the support of the object. Usually, but not always, $s^{R_V}(\lambda) = 0$. In Appendix B, we calculate $s^{R_V}(\lambda)$ for an object of elliptical support.

Finally, the virtual half-line-integrals g^{R_V} must be expressed in terms of acquisition half-line-integrals g^{R_A}. We need $g^{R_V}(\lambda_V, \gamma_V)$ for all $\lambda_V \in \Lambda_{R_V}$, $\gamma \in [-\pi, \pi)$. From the discussion above, we know that the half-line-integral g^{R_V} is equal to the whole line-integral when $\gamma \in \Gamma(s^{R_V}(\lambda))$ so, from (17), we obtain

$$g^{R_V}(\lambda_V, \gamma_V) = \begin{cases} p(\lambda_V + \gamma_V, -R_V \sin\gamma_V) & \text{if } \gamma_V \in \Gamma(s^{R_V}(\lambda)), \\ 0 & \text{if } \gamma_V \in [-\pi, \pi) \setminus \Gamma(s^{R_V}(\lambda)). \end{cases} \quad (34)$$

The $p(\lambda_V + \gamma_V, -R_V \sin\gamma_V)$ value is obtained by averaging the two measurements available from the acquisition projections $g^{R_A}(\lambda_1, \gamma_1)$ and $g^{R_A}(\lambda_2, \gamma_2)$ with the particular values $\phi = \lambda_V + \gamma_V$, $s = -R_V \sin\gamma_V$. From (13)

$$\lambda_1 = \lambda_V + \gamma_V + \pi + \arcsin\left(\tfrac{R_V}{R_A}\sin\gamma_V\right), \qquad \gamma_1 = -\arcsin\left(\tfrac{R_V}{R_A}\sin\gamma_V\right), \quad (35a)$$

$$\lambda_2 = \lambda_V + \gamma_V - \arcsin\left(\tfrac{R_V}{R_A}\sin\gamma_V\right), \qquad \gamma_2 = \arcsin\left(\tfrac{R_V}{R_A}\sin\gamma_V\right), \quad (35b)$$

so, from (14), we obtain, for $\lambda_V \in \Lambda_V$ and $\gamma_V \in \Gamma(s^{R_V}(\lambda))$,

$$\begin{aligned} g^{R_V}(\lambda_V, \gamma_V) &= p(\lambda_V + \gamma_V, -R_V \sin\gamma_V) \\ &= \tfrac{1}{2}\left(g^{R_A}(\lambda_V + \gamma_V + \pi + \gamma_A^V, -\gamma_A^V) + g^{R_A}(\lambda_V + \gamma_V - \gamma_A^V, \gamma_A^V)\right) \end{aligned} \quad (36)$$

where

$$\gamma_A^V = \arcsin\left(\frac{R_V}{R_A}\sin\gamma_V\right). \quad (37)$$

2.6. Reconstruction formulas using the VFB method

We will now present our five VFB formulas. The first three formulas are known SSS formulas (Noo et al. 2002) applied to the virtual trajectory. On the other hand, the last two formulas, which perform backprojection in the acquisition geometry, use the virtual trajectory only when filtered data are not available from the non-truncated acquisition projections.

The condition for reconstruction of $f(\vec{x})$ with a SSS formula is that every line through $\vec{x}$ intersects the fan-beam trajectory to which the SSS formula is applied. For a connected SSS trajectory, this condition is satisfied by any point in the convex hull of the trajectory. As the virtual trajectory is connected (composed of one arc), the reconstruction area for the three first VFB formulas is the convex hull of the virtual trajectory, denoted $\mathrm{conv}(R_V\vec{\theta}_{\Lambda_{R_V}})$.

For the last two formulas, $f(\vec{x})$ can be reconstructed if any line through $\vec{x}$ intersects either the virtual trajectory, or the part of acquisition trajectory with non-truncated projections. So the reconstruction area is larger than for the three previous formulas. Nevertheless, if we restrict our attention to the portion of reconstruction area situated inside the object support, it is the same for all five formulas. (The reason is that any line covered by the one or two arcs of non-truncated acquisition trajectory and passing through the object intersects the virtual trajectory. We do not give a demonstration, but it can be seen from figure 1. So using the non-truncated part of acquisition trajectory in addition of the virtual trajectory does not increase the reconstruction area inside the object support.) We call this area the region-of-interest (ROI) in the following, and we have $\mathrm{ROI} = \Omega \cap \mathrm{conv}(R_V\vec{\theta}_{\Lambda_{R_V}})$ with Ω the elliptic support of the object.

2.6.1. Formulas with parallel backprojection

The first two reconstruction formulas are based on the standard parallel-beam FBP formula, (8), for $\vec{x} \in \mathrm{ROI}$:

$$f(\vec{x}) = \int_0^\pi \left[p_F(\phi, s)\right]\big|_{s=\vec{x}\cdot\vec{\eta}_\phi} \mathrm{d}\phi \tag{38}$$

and the difference between the two formulas is how the filtered projections $p_F(\phi, s)$ are obtained.

In the first case, which we call formula **(a)**, the filtered parallel projections are obtained from Hilbert-transformed parallel projections (equation (7))

$$p_F(\phi, s) = \frac{1}{2\pi}\frac{\partial}{\partial s} p_H(\phi, s) \quad \phi \in [0, \pi),\ s = \vec{x}\cdot\vec{\eta}_\phi \text{ with } \vec{x} \in \mathrm{ROI} \tag{39}$$

and the values of $p_H(\phi, s)$ are obtained through the available filtered virtual projections $g_H^{R_V}$ using (19a) and (19b):

$$p_H(\phi, s) = \quad g_H^{R_V}(\lambda_1^{R_V}, \gamma_1^{R_V}) \quad \text{if } \lambda_1^{R_V} \in \Lambda_{R_V}, \tag{40a}$$

$$= -\, g_H^{R_V}(\lambda_2^{R_V}, \gamma_2^{R_V}) \quad \text{if } \lambda_2^{R_V} \in \Lambda_{R_V}. \tag{40b}$$

Here we introduce the superscript R_V as a reminder that λ_1 and λ_2 lie on the virtual trajectory, so

$$\lambda_1^{R_V}(\phi,s) = \phi + \pi - \arcsin(s/R_V), \qquad \gamma_1^{R_V}(s) = \arcsin(s/R_V) \tag{41a}$$
$$\lambda_2^{R_V}(\phi,s) = \phi + \arcsin(s/R_V), \qquad \gamma_2^{R_V}(s) = -\arcsin(s/R_V) \tag{41b}$$

and for simpler notation, we usually drop the implied (ϕ, s) dependence.

Since we only need $p_H(\phi,s)$ for $\phi \in [0,\pi)$, $s = \vec{x}\cdot\vec{\eta}_\phi$ with $\vec{x} \in \text{ROI} \subset \text{conv}(R_V\vec{\theta}_{\Lambda_{R_V}})$, we are thus assured that either $\lambda_1^{R_V} \in \Lambda_{R_V}$ or $\lambda_2^{R_V} \in \Lambda_{R_V}$. If both $\lambda_1^{R_V}, \lambda_2^{R_V} \in \Lambda_{R_V}$, then, in our implementation, we average the two available values and use

$$p_H(\phi,s) = \tfrac{1}{2}\left(g_H^{R_V}(\lambda_1^{R_V},\gamma_1^{R_V}) - g_H^{R_V}(\lambda_2^{R_V},\gamma_2^{R_V})\right) \quad \text{if } \lambda_1^{R_V} \text{ and } \lambda_2^{R_V} \in \Lambda_{R_V}. \tag{40c}$$

Finally, $g_H^{R_V}$ is computed according to its definition, (10), from g^{R_V} which is found from the acquisition projections g^{R_A}, according to (36).

Note that the virtual trajectory is essential here, because (10) requires non-truncated projections.

In the second case, which we call formula **(b)**, the same parallel geometry FBP formula is used, (38), but this time the filtered parallel projections p_F are obtained directly from the filtered virtual fan-beam projections $g_F^{R_V}$ using (21a) and (21b):

$$p_F(\phi,s) = -\tfrac{1}{\sqrt{R_V^2-s^2}} g_F^{R_V}(\lambda_1^{R_V},\gamma_1^{R_V}) \quad \text{if } \lambda_1^{R_V} \in \Lambda_{R_V}, \tag{42a}$$
$$= -\tfrac{1}{\sqrt{R_V^2-s^2}} g_F^{R_V}(\lambda_2^{R_V},\gamma_2^{R_V}) \quad \text{if } \lambda_2^{R_V} \in \Lambda_{R_V}, \tag{42b}$$

and, for our implementations,

$$p_F(\phi,s) = -\tfrac{1}{2\sqrt{R_V^2-s^2}}\left(g_F^{R_V}(\lambda_1^{R_V},\gamma_1^{R_V}) + g_F^{R_V}(\lambda_2^{R_V},\gamma_2^{R_V})\right) \quad \text{if } \lambda_1^{R_V} \text{ and } \lambda_2^{R_V} \in \Lambda_{R_V}. \tag{42c}$$

As with formula (a), we are assured that at least one of $\lambda_1^{R_V}, \lambda_2^{R_V}$ lies on the virtual trajectory Λ_{R_V} because (ϕ, s) satisfy $\vec{x}\cdot\vec{\eta}_\phi = s$ with $\vec{x} \in \text{ROI} \subset \text{conv}(R_V\vec{\theta}_{\Lambda_{R_V}})$, and thus the line defined by (ϕ, s) will intersect the virtual trajectory.

Finally, $g_F^{R_V}$ is computed from its definition, (11), with g^{R_V} obtained from the acquisition projections g^{R_A}, according to (36).

Note that formulas (a) and (b) amount to the two rebinning methods described by Noo et al. (2002), but applied to the virtual trajectory instead of the non-truncated acquisition projections in (Noo et al. 2002). These two formulas have already been presented by Noo et al. (2002), but the equations for the different steps were not provided, and only the first formula was implemented, with parallel-beam acquisition data instead of fan-beam acquisition data. Moreover, the virtual radius used by Noo et al. (2002) was larger than the FOV radius R_F, so the ROI was not as big as the one obtained in this paper. Thus, we consider the rebinning procedure composed of (34) and (36), allowing the use of R_F as virtual radius to obtain the largest possible ROI for the VFB method in the context of unilateral truncation, to be a new contribution.

2.6.2. Formula with fan-beam backprojection in the virtual geometry

The third reconstruction formula is based on the fan-beam SSS formula (32) described by Noo et al. (2002), but applied to the virtual trajectory instead of the acquisition trajectory, since it requires non-truncated projections. This formula, called **(c)**, is defined for $\vec{x} \in$ ROI, with $\vec{x}$ verifying the additional constraint $||\vec{x}|| < R_V$, and given by (32) with the virtual trajectory:

$$f(\vec{x}) = -\int_{\Lambda_{R_V}} \frac{1}{||\vec{x} - R_V\vec{\theta}_\lambda||} \left[w^{R_V}(\lambda,\gamma) g_F^{R_V}(\lambda,\gamma)\right]\Big|_{\gamma=\gamma_{\vec{x},\lambda}^{R_V}} \mathrm{d}\lambda. \tag{43}$$

As in formula (b), $g_F^{R_V}$ is computed from its definition (11) with g^{R_V} obtained through (36). The values of $\gamma_{\vec{x},\lambda}^{R_V}$ and w^{R_V} are given respectively in equations (30) and (33).

As with formulas (a) and (b), formula (c) is not in itself a new formula, but the rebinning procedure common to these three formulas can be considered new.

2.6.3. Formulas with fan-beam backprojection in the acquisition geometry

We now develop two formulas with fan-beam backprojection in the acquisition geometry. They are based on the fan-beam SSS formula (32) and their common backprojection step is, for $\vec{x} \in$ ROI:

$$f(\vec{x}) = -\int_0^{2\pi} \frac{1}{||\vec{x} - R_A\vec{\theta}_\lambda||} \left[\widetilde{w}^{R_A}(\lambda,\gamma) \widetilde{g}_F^{R_A}(\lambda,\gamma)\right]\Big|_{\gamma=\gamma_{\vec{x},\lambda}^{R_A}} \mathrm{d}\lambda \tag{44}$$

where $\widetilde{w}^{R_A}$ and $\widetilde{g}_F^{R_A}$ are specified below for each formula. Unlike formula (c), filtered projections are here computed from their definition (11) only on the portion $\Lambda_{R_A}^C$ of acquisition trajectory, for which there is no truncation. For the remaining portion $\Lambda_{R_A}^T$ of the acquisition trajectory, we will show that some values of $g_F^{R_A}$ are accessible thanks to a link between $g_F^{R_A}$ and $g_F^{R_V}$. (The accessible values will correspond to when $g_F^{R_V}$ can be computed, i.e. to the rays intersecting the virtual trajectory.) This link will be expressed first with explicit rebinning steps between the virtual and acquisition geometries. Then it will be rewritten to obtain an expression of $g_F^{R_A}$ directly in terms of g^{R_A}, in a manner that avoids using the missing data. So in the first case, which we call formula **(d)**, the filtered acquisition projections are obtained from

$$\widetilde{g}_F^{R_A}(\lambda,\gamma) = \begin{cases} g_F^{R_A}(\lambda,\gamma) & \text{if } \lambda \in \Lambda_{R_A}^C, \\ \bar{g}_F^{R_A}(\lambda,\gamma) & \text{if } \lambda \text{ and } \lambda+\pi+2\gamma \in \Lambda_{R_A}^T, \text{ and } \lambda+\gamma-\gamma_V^A \in \Lambda_{R_V}, \\ 0 & \text{else,} \end{cases} \tag{45}$$

where $\bar{g}_F^{R_A}$ represents $g_F^{R_A}$ obtained from $g_F^{R_V}$ with explicit rebinning steps between acquisition and virtual geometries, while in the second case, which we call formula **(e)**, the filtered acquisition projections are obtained from

$$\widetilde{g}_F^{R_A}(\lambda,\gamma) = \begin{cases} g_F^{R_A}(\lambda,\gamma) & \text{if } \lambda \in \Lambda_{R_A}^C, \\ \bar{\bar{g}}_F^{R_A}(\lambda,\gamma) & \text{if } \lambda \text{ and } \lambda+\pi+2\gamma \in \Lambda_{R_A}^T, \text{ and } \lambda+\gamma-\gamma_V^A \in \Lambda_{R_V}, \\ 0 & \text{else.} \end{cases} \tag{46}$$

where $\bar{\bar{g}}_F^{R_A}$ is a rewriting of $\bar{g}_F^{R_A}$ to have $g_F^{R_A}$ expressed directly from the available acquisition data g^{R_A}.

In those twos formulas, $\bar{g}_F^{R_A}$ and $\bar{\bar{g}}_F^{R_A}$ are used only when $\lambda \in \Lambda_{R_A}^T$, $\lambda+\pi+2\gamma \in \Lambda_{R_A}^T$, and $\lambda+\gamma-\gamma_V^A \in \Lambda_{R_V}$. Among those three requirements, the first one is obvious since if $\lambda \in \Lambda_{R_A}^C$, we can compute $g_F^{R_A}$ directly from its definition. The second one is due to the redundancy of the filtered data $g_F^{R_A}(\lambda,\gamma)$ and $g_F^{R_A}(\lambda+\pi+2\gamma,-\gamma)$. It follows that if $\lambda+\pi+2\gamma \in \Lambda_{R_A}^C$ then $g_F^{R_A}(\lambda,\gamma)$ is already taken into account directly from the acquisition trajectory, so $\bar{g}_F^{R_A}$ and $\bar{\bar{g}}_F^{R_A}$ are needed only when $\lambda+\pi+2\gamma \in \Lambda_{R_A}^T$. (This requirement will also make easier the redundancy handling, as shown below.) Finally, the condition $\lambda+\gamma-\gamma_V^A \in \Lambda_{R_V}$ is needed to ensure that the fan-beam ray parameterized by (λ,γ) in the acquisition geometry intersects the virtual trajectory, so that the link between $g_F^{R_A}$ and $g_F^{R_V}$ can be used.

Before expressing $\bar{g}_F^{R_A}$ and $\bar{\bar{g}}_F^{R_A}$, we focus on the redundancy weight $\widetilde{w}^{R_A}$, which will be the same for both formulas. The requirement that $\lambda+\pi+2\gamma$ belongs to $\Lambda_{R_A}^T$ - to use $\bar{g}_F^{R_A}$ and $\bar{\bar{g}}_F^{R_A}$ - ensures that there is not redundancy between $g_F^{R_A}$ computed directly and $g_F^{R_A}$ obtained from $\bar{g}_F^{R_A}$ or $\bar{\bar{g}}_F^{R_A}$, so the redundancy can be treated separately in each case. For $\lambda \in \Lambda_{R_A}^C$, both formulas use the non-truncated acquisition projections so the redundancy can be handled with w^{R_A}, defined as w^R applied to $\Lambda_R = \Lambda_{R_A}^C$. For λ and $\lambda+\pi+2\gamma \in \Lambda_{R_A}^T$, $\bar{g}_F^{R_A}$ and $\bar{\bar{g}}_F^{R_A}$ provide filtered data only for rays intersecting the virtual trajectory, so the redundancy can be handled in the virtual setting with w^{R_V}, which amounts to use $w^{R_V}(\lambda+\gamma-\gamma_V^A,\gamma_V^A)$ when we rebin back into the acquisition setting. Thus the total redundancy weight is given by

$$\widetilde{w}^{R_A}(\lambda,\gamma) = \begin{cases} w^{R_A}(\lambda,\gamma) & \text{if} \quad \lambda \in \Lambda_{R_A}^C, \\ w^{R_V}(\lambda+\gamma-\gamma_V^A,\gamma_V^A) & \text{if} \quad \lambda \text{ and } \lambda+\pi+2\gamma \in \Lambda_{R_A}^T, \\ 0 & \text{else,} \end{cases} \tag{47}$$

where w^{R_A} is obtained by applying the definition of w^R, (33), to $\Lambda_{R_A}^C$, the portion of acquisition trajectory with non-truncated projections. For the first parameter of w^{R_V}, we implicitly consider its value modulo 2π when it is outside $[0,2\pi)$.

We now discuss $\bar{g}_F^{R_A}$, the key element of method (d). It is based on the following result (proven below):

Proposition 1
For two circular trajectories of radius R_A and R_V, with $R_V \leq R_A$, $\gamma_V \in (-\pi/2,\pi/2)$, and $\gamma_A \in (-\gamma_m,\gamma_m)$ where $\gamma_m = \arcsin(R_V/R_A)$, we have

$$\frac{g_F^{R_A}(\lambda_A,\gamma_A)}{R_A\cos(\gamma_A)} = \frac{g_F^{R_V}(\lambda_V,\gamma_V)}{R_V\cos(\gamma_V)} \tag{48}$$

where

$$\begin{array}{rcl} R_A\sin\gamma_A &=& R_V\sin\gamma_V, \\ \lambda_A+\gamma_A &=& \lambda_V+\gamma_V. \end{array} \tag{49}$$

Then, from (49), we can express the virtual geometry parameters in terms of the acquisition geometry parameters: $\gamma_V = \arcsin((R_A/R_V)\sin\gamma_A)$ and $\lambda_V =$

$\lambda_A + \gamma_A - \gamma_V = \lambda_A + \gamma_A - \arcsin((R_A/R_V)\sin\gamma_A)$. It follows that $R_V \cos\gamma_V = R_V \cos\arcsin((R_A/R_V)\sin\gamma_A) = R_V\sqrt{1-((R_A/R_V)\sin\gamma_A)^2} = \sqrt{R_V^2 - R_A^2\sin^2\gamma_A}$. So, combining (48) with (49), we obtain the following result:

Corollary 1
Consider two circular trajectories of radius R_A and R_V, with $R_V \leq R_A$ and $\gamma_m = \arcsin(R_V/R_A)$. Then, for all $\lambda \in [0, 2\pi)$ and all $\gamma \in (-\gamma_m, \gamma_m)$ such that $\lambda + \gamma - \gamma_V^A \in \Lambda_{R_V}$, we have

$$\bar{g}_F^{R_A}(\lambda,\gamma) = \frac{R_A\cos\gamma}{\sqrt{R_V^2 - R_A^2\sin^2\gamma}} g_F^{R_V}(\lambda+\gamma-\gamma_V^A, \gamma_V^A) \tag{50}$$

where

$$\gamma_V^A = \arcsin\left(\frac{R_A}{R_V}\sin\gamma\right). \tag{51}$$

We use the alternative notation $\bar{g}_F^{R_A}$ instead of $g_F^{R_A}$ to emphasize that the filtered acquisition projections are not obtained through the definition (11).

We now demonstrate proposition 1. It is a consequence of (21), which shows that for any radius $R > 0$, the fan-beam filtered projection g_F^R can be related to the parallel-beam filtered projection p_F. So a link can be established between any pair of filtered data $(g_F^{R_1}, g_F^{R_2})$ for any two positive radius R_1 and R_2. Starting from (21*a*), we have, for all $\phi \in [0, 2\pi)$ and all $s \in (-R, R)$, $p_F(\phi, s) = -g_F^R(\lambda_1, \gamma_1)/\sqrt{R^2 - s^2}$ where, as usual, $\lambda_1 = \phi + \pi - \arcsin(s/R)$ and $\gamma_1 = \arcsin(s/R)$. It follows, for all $\lambda \in [0, 2\pi)$ and all $\gamma \in (-\pi/2, \pi/2)$,

$$p_F(\lambda+\gamma-\pi, R\sin\gamma) = -\frac{1}{R\cos\gamma} g_F^R(\lambda,\gamma). \tag{52}$$

We can apply the above result to both $R = R_A$ and $R = R_V$. To combine those two relations, we need the parameters of p_F to have the same value in both cases, hence $s = R_A\sin\gamma_A = R_V\sin\gamma_V$ and $\phi = \lambda_A + \gamma_A - \pi = \lambda_V + \gamma_V - \pi$. With this assumption, we obtain proposition 1.

We now specify $\bar{\bar{g}}_F^{R_A}$, the key element of formula (e). In (50), the filtered acquisition data $g_F^{R_A}$ data are expressed in terms of the filtered virtual data $g_F^{R_V}$, which are defined in (11) from the virtual projections g^{R_V}. Since those virtual projections are obtained from the acquisition projections g^{R_A} through the rebinning relation (36), it is possible to reformulate the previous link (50) between $g_F^{R_A}$ and $g_F^{R_V}$ to express $g_F^{R_A}$ directly from the acquisition projections g^{R_A} in a manner that avoids using the truncated part of the projections.

The main work is to express $g_F^{R_V}$ in terms of g^{R_A}, which is done by combining definition (11) of $g_F^{R_V}$ with the rebinning relation (36) between g^{R_A} and g^{R_V}. To do so, we use the change of variables $\gamma_A = \arcsin\left((R_V/R_A)\sin\gamma_V\right)$ between the acquisition and virtual geometries. To have this change of variables one-to-one, we need the γ-interval of the virtual projections $g^{R_V}(\lambda,\gamma)$ to be contained within $(-\pi/2, \pi/2)$. This is ensured by shifting the initial γ-interval $\Gamma(s^{R_V}(\lambda)) = [-\pi/2 + s^{R_V}(\lambda), \pi/2 + s^{R_V}(\lambda))$ by the

offset angle $s^{R_V}(\lambda)$, for each λ. See Appendix C for a complete demonstration. Thus we obtain the following result:

Proposition 2
Consider two circular trajectories of radius R_A and R_V, with $R_V \leq R_A$ and $\gamma_m = \arcsin(R_V/R_A)$. If the virtual vertex $R_V\vec{\theta}_{\lambda+\gamma-\gamma_V^A}$ is outside the convex hull of the object support (i.e. if $\lambda+\gamma-\gamma_V^A \in \Lambda_{R_V}$, with γ_V^A defined in (51)) then, for all $\lambda \in [0, 2\pi)$ and all $\gamma \in (-\gamma_m, \gamma_m)$, we have

$$\bar{\bar{g}}_F^{R_A}(\lambda,\gamma) = \frac{R_A\cos\gamma}{4\pi\sqrt{R_V^2 - R_A^2\sin^2\gamma}} \int_{-\gamma_m}^{\gamma_m} h_H\left(\sin\left(\gamma_V^A - {\gamma'}_V^A\right)\right) \operatorname{sign}_V^A(\lambda,\gamma,\gamma') \left[\partial g^{R_A}(\lambda+\gamma-\gamma'-(\gamma_V^A-{\gamma'}_V^A),\gamma') - \partial g^{R_A}(\lambda+\pi+\gamma+\gamma'-(\gamma_V^A-{\gamma'}_V^A),-\gamma')\right] \mathrm{d}\gamma' \tag{53}$$

where

$$\partial g^{R_A}(\lambda,\gamma) = \left(\frac{\partial}{\partial\lambda} - \frac{\partial}{\partial\gamma}\right) g^{R_A}(\lambda,\gamma), \tag{54}$$

and

$$\operatorname{sign}_V^A(\lambda,\gamma,\gamma') = \operatorname{sign}\left(\pi/2 - \left|{\gamma'}_V^A - s^{R_V}(\lambda+\gamma-\gamma_V^A)\right|\right). \tag{55}$$

Propositions 1 and 2, as well as formulas (d) and (e), are, to our knowledge, new results. We now analyse the differences between formulas (d) and (e) regarding the way filtered projections are obtained from truncated acquisition projections. We observe two main differences: one concerns the rebinning steps, and the other concerns the filtering step (we consider here the differentiation to be part of the filtering step).

In formula (d), the process of obtaining filtered projections in the acquisition geometry via the virtual geometry consists of three steps: an explicit rebinning of the acquisition projections into virtual projections using (36), a differentiation and filtering of the virtual projections with (11), and an explicit rebinning of the virtual filtered projections into acquisition filtered projections using (50). In formula (e), these three steps are condensed into a single one, (53). Therefore, formula (e) performs only one step of 1D interpolation, on the first variable of ∂g^{R_A} in equation (53) (the second variable of ∂g^{R_A} is evaluated at γ' and $-\gamma'$, which correspond both to discretization values of the second variable of g^{R_A}), while formula (d) performs two steps of 2D interpolation, on both variables of g^{R_A} and $g_F^{R_V}$, in equations (36) and (50) respectively.

In formula (d), the filtering step is performed in the virtual geometry, with (11). In this equation, the first parameter of g^{R_V} is independent of the integration variable γ', so the filtering step of (d) is shift-invariant and corresponds to a convolution. In formula (e), the filtering step is done in (53). When (53) is applied with $R_V \neq R_A$, the first variable of ∂g^{R_A} depends on the integral variable γ', so the filtering step of (e) is shift-variant and does not correspond to a convolution.

2.6.4. Summary of the five VFB formulas

The different steps of the five reconstruction formulas are summarized in figure 4, with each step associated with the corresponding equation, using the following color code: blue for acquisition geometry, red for virtual geometry and green for parallel geometry.

3. Implementation of the formulas

3.1. Rebinning

The rebinning steps are performed through an inverse mapping (Wolberg 1990, Section 3.1.2). Each element of the rebinned projections is mapped into the input projections and computed with bilinear interpolation. In equation (36), the interpolations are performed on the right term, on the acquisition sinogram g^{R_A}, and the acquisition data are not uniformly used. (Virtual and acquisition rays are equally spaced at the center of rotation but their spacings differ elsewhere, such that there are many more virtual samples in total than acquisition samples. Therefore, when stepping uniformly through the virtual samples, the acquisition samples are increasingly accessed when moving closer to the extremities $\pm\gamma_m$.) In equations (50) and (53), the interpolations are also performed on the right term, on $g_F^{R_V}$ and ∂g^{R_A} respectively. On the other hand, no rebinning step is used to get $\widetilde{w}^{R_A}$ (see section 3.4).

3.2. Differentiation

Following (Noo et al. 2002), the differentiation steps are performed with the formulas

$$\frac{\partial}{\partial\lambda}g^R(\lambda,\gamma) \approx \frac{g^R(\lambda+\Delta_\lambda,\gamma) - g^R(\lambda-\Delta_\lambda,\gamma)}{2\Delta_\lambda}, \tag{56}$$

$$\frac{\partial}{\partial\gamma}g^R(\lambda,\gamma) \approx \frac{g^R(\lambda,\gamma+\Delta_\gamma) - g^R(\lambda,\gamma-\Delta_\gamma)}{2\Delta_\gamma}, \tag{57}$$

$$\frac{\partial}{\partial s}p_H(\phi,s) \approx \frac{p_H(\phi,s+\Delta_s) - p_H(\phi,s-\Delta_s)}{2\Delta_s}, \tag{58}$$

where Δ_λ, Δ_γ and Δ_s are the respective discretization steps of parameters λ, γ and s.

3.3. Filtering

We discretize the 'Hilbert sin' filter $h_H \circ \sin$ similarly to the 'ramp sin' filter $h_F \circ \sin$ in (Kak & Slaney 1988, Section 3.4.1), with a rectangular apodization window and obtain

$$h_H^{\text{rect}}(\sin(n\Delta_\gamma)) = \begin{cases} 0 & \text{for n even,} \\ \dfrac{2}{\pi\sin(n\Delta_\gamma)} & \text{for n odd.} \end{cases} \tag{59}$$

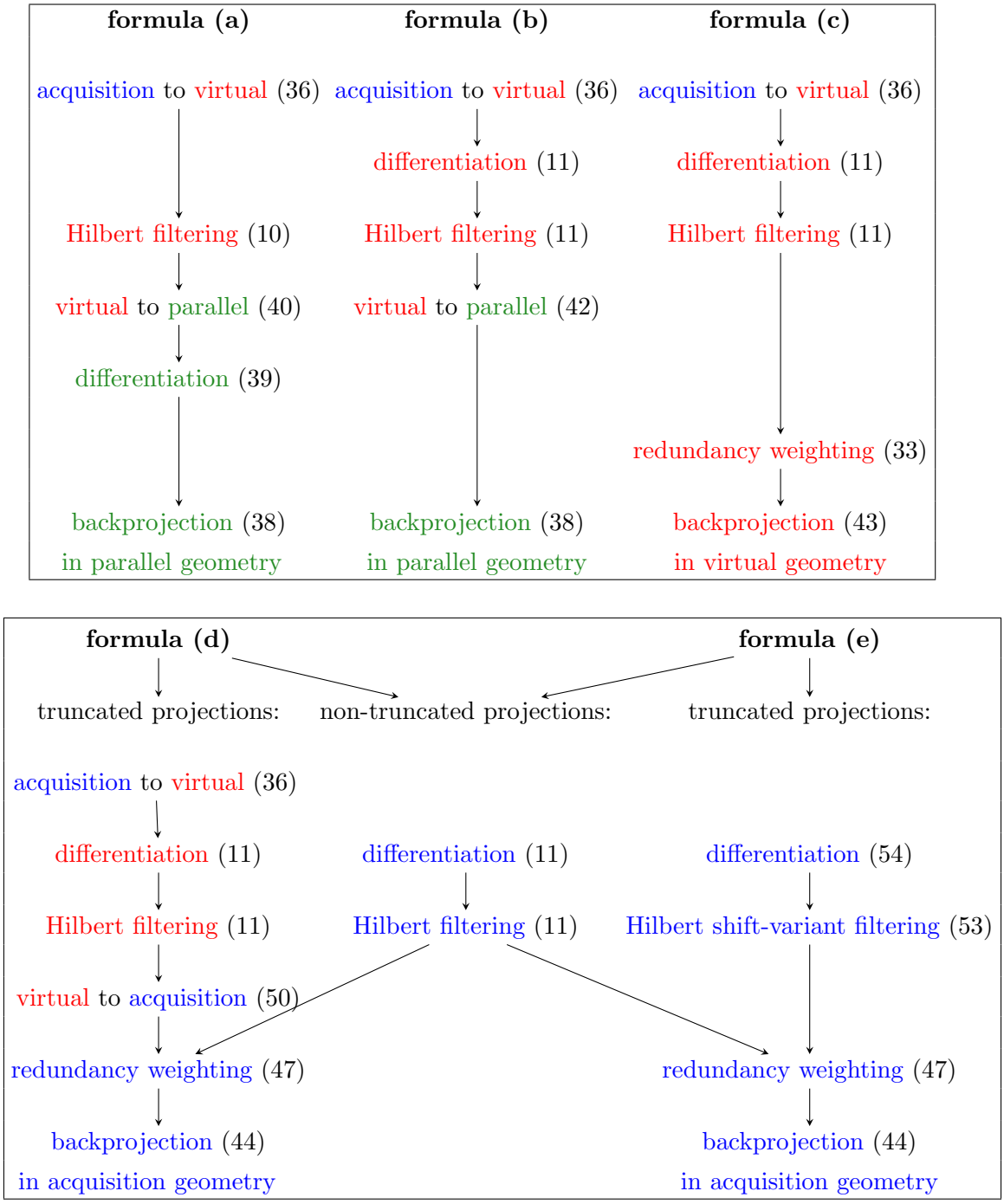

Figure 4. Summary of the different steps of the five VFB formulas. The top block is composed of three already known SSS formulas, applied to the SSS virtual trajectory we chose. The bottom block is composed of the two new VFB formulas we have derived.

In formulas (a), (b), (c) and (d), the filtering step (10) or (11) corresponds to a convolution, which was performed using the fast Fourier transform to reduce the computation time. However, this was not possible for formula (e), as its filtering step (53) does not correspond to a convolution when $R_A \neq R_V$.

3.4. Backprojection

The backprojection step is performed with a pixel-driven approach (inverse mapping). For each pixel of the reconstructed image grid, the data contribution is obtained through linear interpolation of the filtered data. For formulas (c), (d) and (e), the redundancy weights w^{R_V} and $\widetilde{w}^{R_A}$, obtained from equations (33) and (47) respectively, are computed for all rays passing through the pixels of the image grid, without interpolations. On the other hand, for formulas (a) and (b), the redundancy weights are applied to the rays specified by the virtual fan-beam sinogram, before the rebinning step to the parallel geometry (see the right terms in (40) and (42)).

3.5. Computational complexity analysis

In all formulas but (e), the most expensive step is the backprojection. The complexity of parallel backprojection is $O(N_\phi N_x^2)$, with N_ϕ the number of parallel projections and N_x^2 the number of pixels of the reconstructed grid. The complexity of backprojection in the virtual fan-beam geometry is $O(N_{\lambda_V} N_x^2)$, with N_{λ_V} the number of virtual fan-beam projections, and the complexity of backprojection in the acquisition fan-beam geometry is $O(N_{\lambda_A} N_x^2)$, with N_{λ_A} the number of acquisition fan-beam projections (see table 1 for the values of $N_\phi, N_{\lambda_A}, N_{\lambda_V}, N_x$). For the same number of projections, fan-beam backprojection is more expensive than parallel backprojection, due to the computation of the backprojection weight $1/||\vec{x} - R_V\vec{\theta}_\lambda||$.

For formula (e), the most expensive step is the shift-variant filtering. Since it cannot be performed with fast Fourier transform (FFT) (which allows a convolution with a $O(N_{\lambda_A} N_{\gamma_A} \log N_{\gamma_A})$ complexity), its complexity is $O(N_{\lambda_A} N_{\gamma_A}^2)$, with N_{γ_A} the number of rays in each fan-beam acquisition projection.

4. Simulations and results

4.1. Numerical simulations

We simulate four scanning configurations: two with full data acquisition of a 2D slice of the Forbild head phantom (Lauritsch & Bruder) (figures 5 (a) and (b)) and two with truncated acquisitions of a 2D slice of either the Forbild head phantom (figure 6 (a)) or the Forbild thorax phantom (Sourbelle) (figure 6 (b)).

The acquisition trajectory under consideration is the outer dashed circle of radius R_A. Fan-beam projections are acquired (simulated) such that only the rays passing through the inner dashed circle of radius R_F are measured (the FOV is the disk inside this inner circle). In configuration 1, the chosen virtual trajectory is the circle of radius R_A (which corresponds to the acquisition trajectory) while in configuration 2, the virtual trajectory is the circle of radius R_F (which corresponds to the border of the FOV). For both configurations, no truncation of the head phantom occurs. Configuration 2 is used to study the artefacts induced by the rebinning steps between two circular trajectories

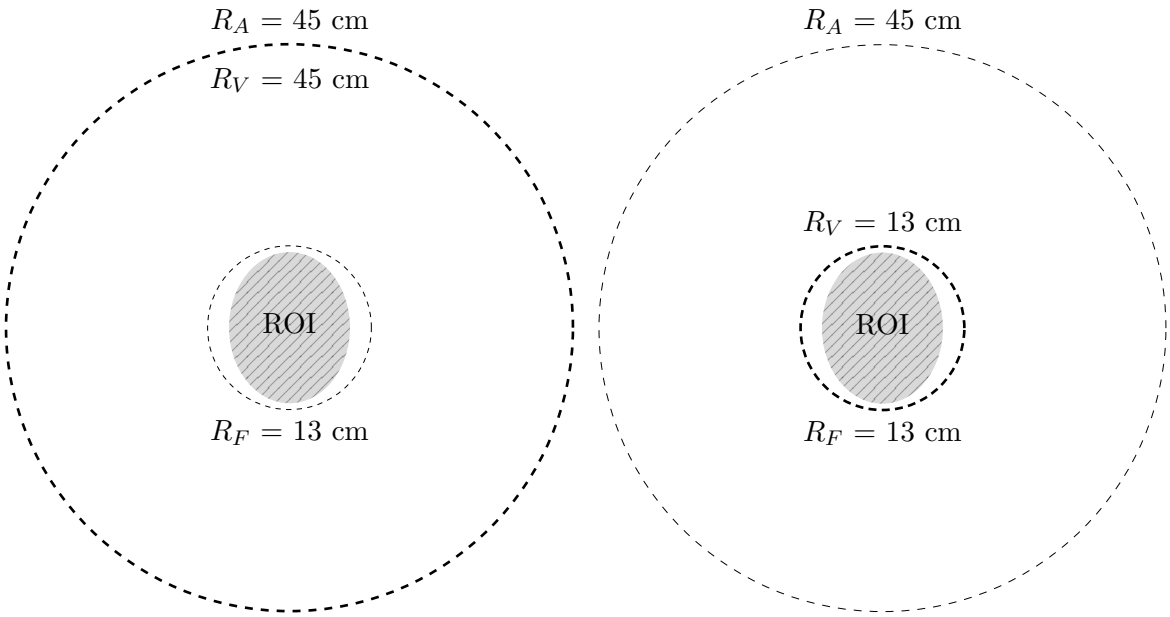

(a) configuration 1 (b) configuration 2

Figure 5. Two configurations with full data acquisition of the 2D slice at z=0 of the Forbild head phantom centered at (0, 0), for a circular source trajectory of center (0,0) and radius $R_A = 45$, and a FOV of center (0,0) and radius $R_F = 13$. We choose for virtual trajectory the circle of center (0,0) and radius $R_V = R_A = 45$ (left) and $R_V = R_F = 13$ (right) (bold dashed circle). The ROI (striped area) is the full object. (all values in cm)

with different radii, without the influence of truncation, which will be studied in the following configurations. In configurations 3 and 4, the largest ROI is obtained by choosing the virtual trajectory to be the arc of the inner circle outside the convex hull of object support (which corresponds to the border of the FOV outside the convex hull of the object support), i.e $R_V = R_F$ as in configuration 2. In figures 5 and 6, the virtual trajectory is represented by a bold dashed (arc of) circle and the ROI is the striped area. In figure 6, the non-truncated part of the acquisition trajectory is represented by a thick dotted arc of circle.

The data were acquired with an acquisition trajectory of radius $R_A = 45$ cm for all configurations. The reconstructed images were computed on a square grid of dimensions $[-x_{\text{extent}}, x_{\text{extent}}]$ in each direction with $x_{\text{extent}} = R_F$, $\Delta_x = 0.04$ cm and $N_x = 2x_{\text{extent}}/\Delta_x + 1$. We let N_{λ_A}, N_{λ_V}, N_{γ_A} and N_{γ_V} represent the number of vertices and of equiangular rays of the acquisition and virtual trajectories respectively, and N_ϕ and N_s the number of parallel projections and parallel rays used in formulas (a) and (b). From Natterer (1986, Section III.3), we can determine the optimal values of these numbers for the reconstruction of a function f of support $[-x_{\text{extent}}, x_{\text{extent}}] \times [-x_{\text{extent}}, x_{\text{extent}}]$ on a Cartesian grid of step Δ_x. We obtain $\Delta_\lambda = \Delta_x/x_{\text{extent}}$, $\Delta_\gamma \approx \Delta_x/R$ with R the radius of the fan-beam trajectory considered (Δ_γ is such that the spacing between two rays at the center of rotation is equal to Δ_x), $\Delta_\phi = \Delta_x/x_{\text{extent}}$ and $\Delta_s = \Delta_x$, from which we can compute the number of projections and rays in each geometry. The values used in

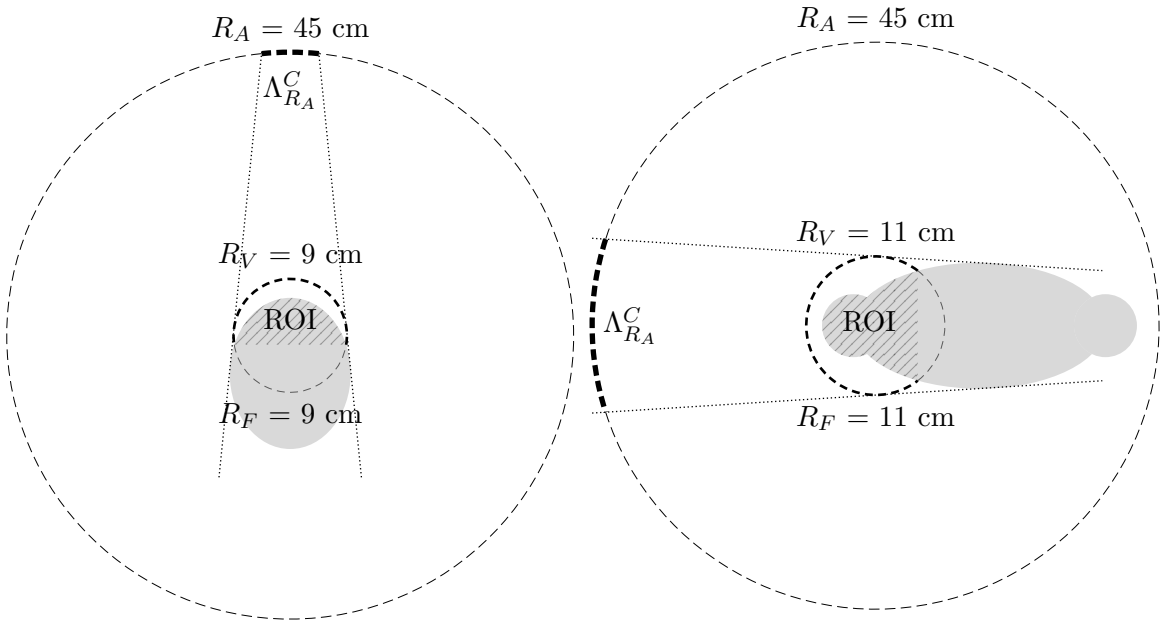

(a) configuration 3 (b) configuration 4

Figure 6. Two situations with truncated data acquisition, for a circular acquisition source trajectory of center (0,0) and radius $R_A = 45$. The tangents to the object and the FOV delimit the part of the trajectory for which the projections are non-truncated (thick dashed arc of circle of radius R_A and of angular extent $\Lambda^C_{R_A}$). We display the ROI (striped area) in case of a virtual trajectory of radius $R_V = R_F$ (bold dashed arc of circle), for respectively the 2D slice at z=0 of the Forbild head phantom centered at (0, -6) with a FOV of center (0,0) and radius $R_F = 9$ (left) and the 2D slice at z=14.1 of the Forbild thorax phantom centered at (16.5, 0) with a FOV of center (0,0) and radius $R_F = 11$ (right). (all values in cm)

the four configurations are summarized in table 1.

Table 1. Sampling values used for the reconstructions of the four configurations.

configuration	1	2	3	4
R_A (in cm)	45	45	45	45
R_V (in cm)	45	13	9	11
$R_F = x_{\text{extent}}$ (in cm)	13	13	9	11
N_{λ_A}	2042	2042	1414	1728
N_{γ_A}	661	661	455	557
N_{λ_V}	2042	2042	780	1225
N_{γ_V}	661	1020	1412	1728
N_ϕ	1020	1020	708	864
$N_s = N_x$	651	651	451	551

The sinograms were computed using RTK (Rit et al. 2014). To avoid high-frequency artefacts due to the sharpness of the phantoms, we smoothed the sinogram entries by computing 3 rays per pixel and averaging those 3 values for each detector pixel.

4.2. Results

We compare our five VFB formulas (a), (b), (c) (d), (e) and we add, as reference for the non-truncated configurations, the fan-beam FBP formula (see (Kak & Slaney 1988) for instance)

$$f(\vec{x}) = \frac{1}{2}\int_0^{2\pi} \frac{1}{||\vec{x} - R_A\vec{\theta}_\lambda||^2} \int_{-\frac{\pi}{2}}^{\frac{\pi}{2}} h_F(\sin(\gamma^{R_A}_{\vec{x},\lambda} - \gamma'))R_A \cos\gamma' g^{R_A}(\lambda,\gamma')\mathrm{d}\gamma'\mathrm{d}\lambda \quad (60)$$

where $\gamma^R_{\vec{x},\lambda}$ is defined in (30). The reference 2D slices of the head and thorax phantom, both centered at (0,0), are shown in figure 7.

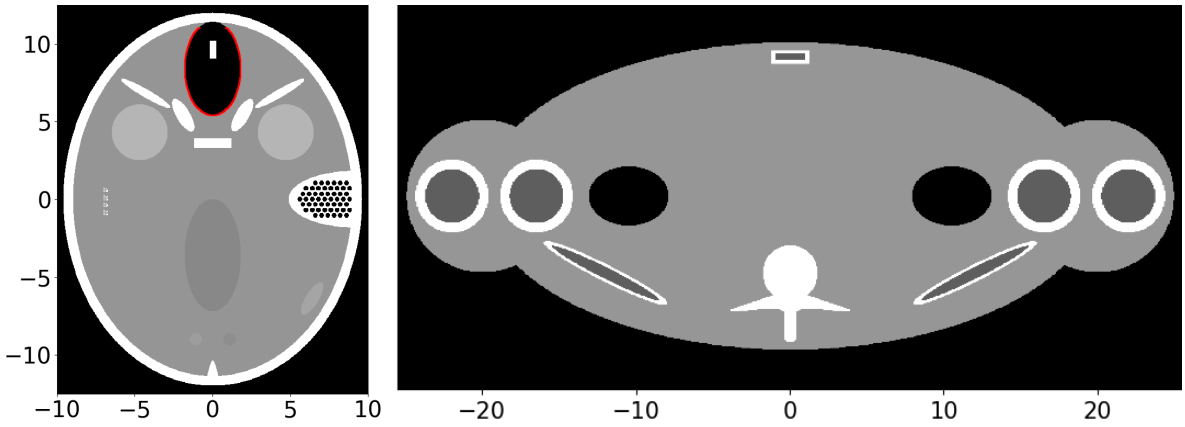

Figure 7. 2D reference slices of the head phantom (left) and the thorax phantom (right). The red ellipse drawn on the head phantom is the interface used to evaluate the spatial resolution.

4.2.1. Noise-free case

In this section, we used noiseless sinograms. Figure 8 shows, for the non-truncated configurations 1 (top) and 2 (bottom), the reconstructed images of the fan-beam FBP and the five VFB formulas. Figures 9 and 10 show, for the truncated configurations 3 and 4 respectively, the reconstructed images and the corresponding profiles of the fan-beam FBP and the five VFB formulas.

For configuration 1, the six reconstructions are rather similar. The only remarkable artefacts are horizontal streaks passing through the inner right ear (right white half-ellipse containing black disks in figure 7 left), which are present in formulas (a), (b) and (c).

For configuration 2, other artefacts appear for formulas (a), (b) and (c). We now see many streaks, which are stronger for (b) than for (a) and (c). For (c), two other kinds of artefacts can be observed : a thin ring of white artefacts surrounding the trajectory, and a black and white pattern at the bottom of the head. Note that the four reconstructions of formulas (d) and (e) in configurations 1 and 2 are all the same, as there is no truncation of the acquisition data (recall from figure 4 that (d) et (e) perform

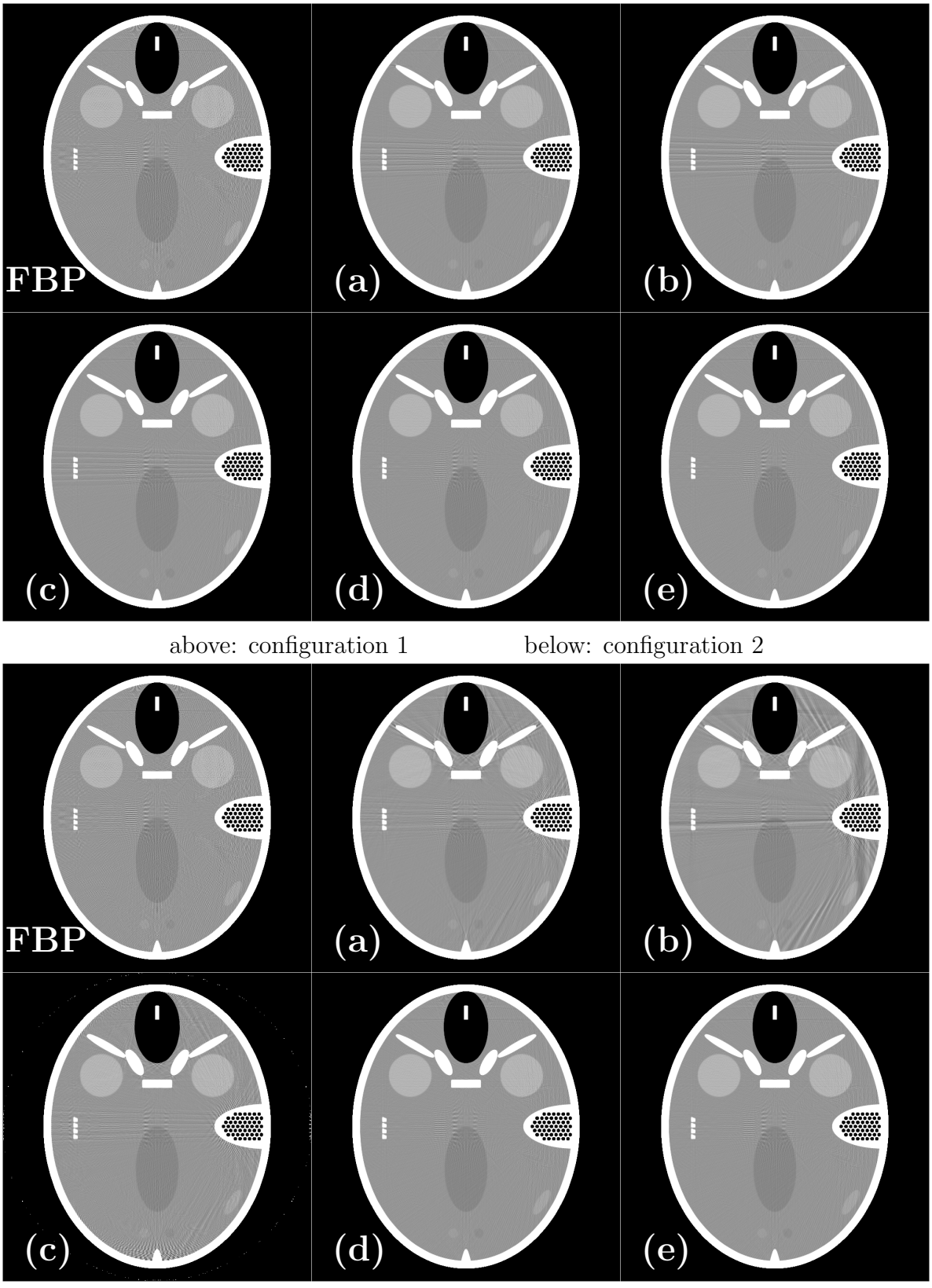

Figure 8. Top rows: images reconstructed from the head phantom with $R_V = 45$ cm (configuration 1) for the fan-beam FBP and the five VFB formulas. Bottom rows: images reconstructed from the head phantom with $R_V = 13$ cm (configuration 2) for the FBP and the five VFB formulas. The plotting scale is [1 (black), 1.1 (white)]. In both cases, there is no truncation of acquisition data, so both FBP reconstruction are the same, and the four reconstructions of formulas (d) and (e) are all the same.

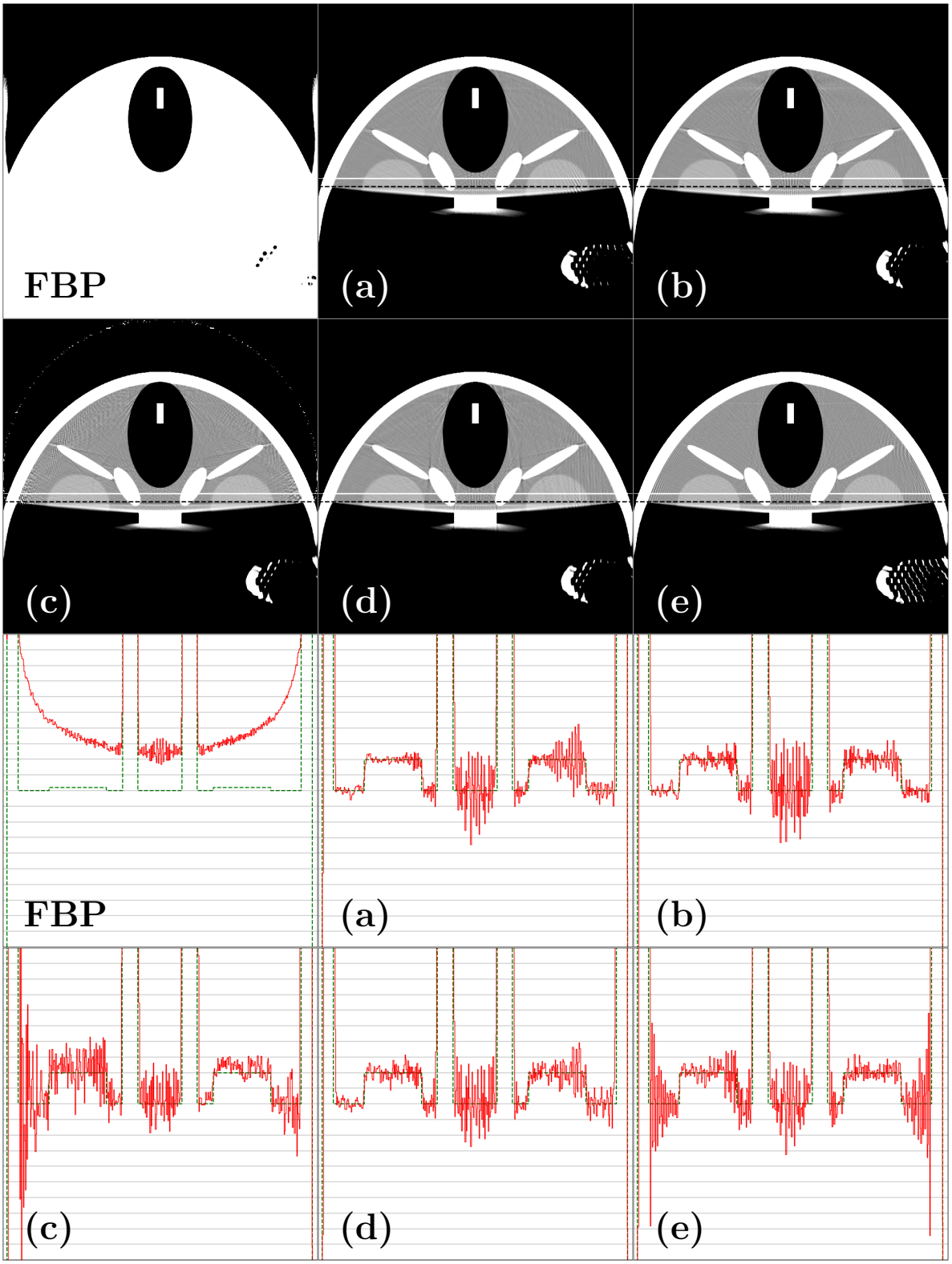

Figure 9. Top rows: images reconstructed from the head phantom with $R_V = 9$ cm (configuration 3) for the naive fan-beam FBP and the five VFB formulas. The horizontal black dashed line defines the boundary of the possible reconstruction area. The plotting scale is [1 (black), 1.1 (white)]. Bottom rows: profiles corresponding to the white horizontal line, plotted with scale [1, 1.1] for the VFB formulas and scale [0.55, 1.55] for the fan-beam FBP. The reference profiles are plotted in green dashed line and the reconstruction profiles in red.

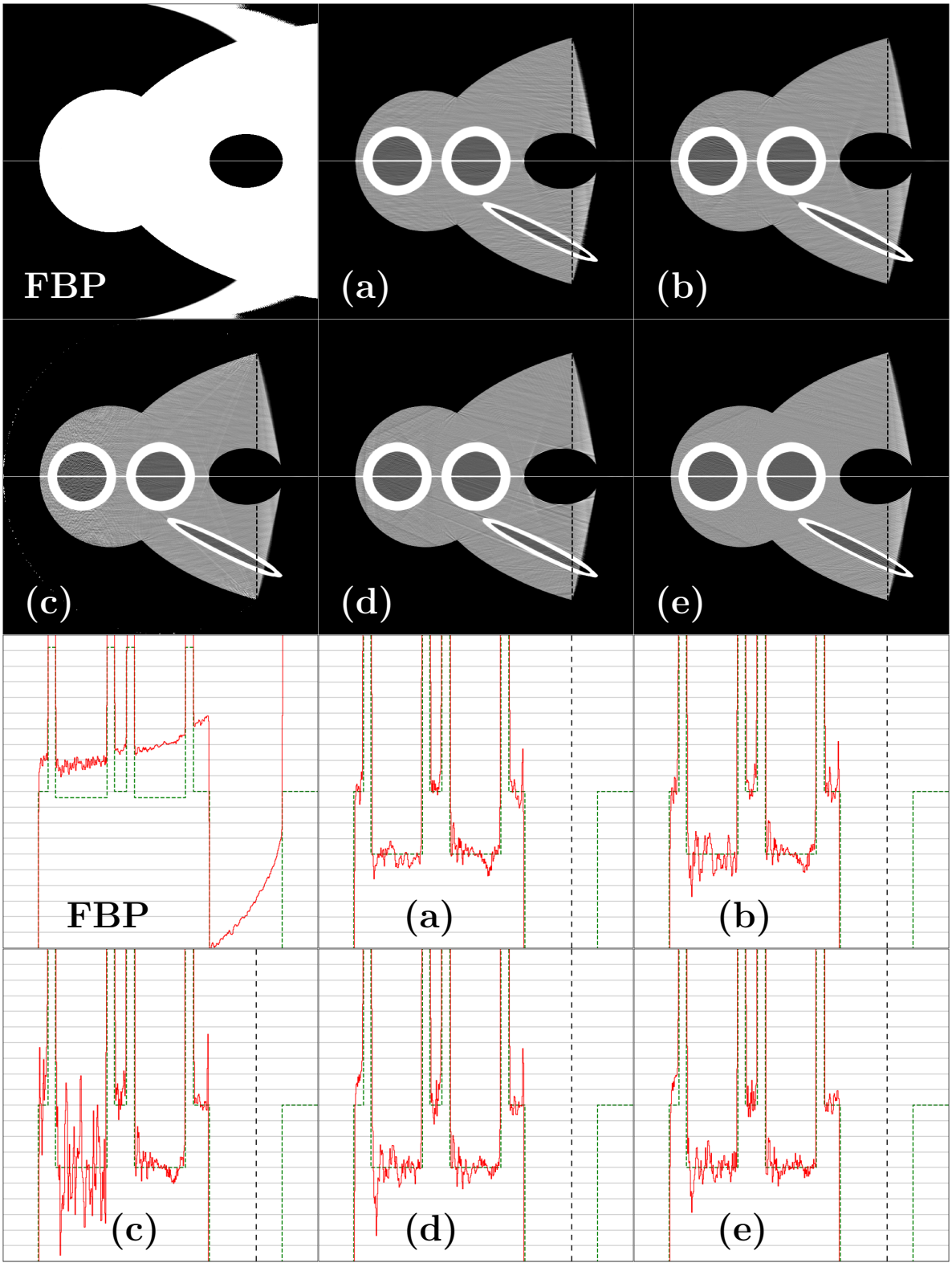

Figure 10. Top rows: images reconstructed from the thorax phantom with $R_V = 11$ cm (configuration 4) for the naive fan-beam FBP and the five VFB formulas. The vertical black dashed line defines the boundary of the possible reconstruction area. The plotting scale is [0.95 (black), 1.05 (white)]. Bottom rows: profiles corresponding to the white horizontal line, plotted with scale [0.95, 1.05] for the VFB formulas and scale [0.5, 1.5] for the fan-beam FBP. The reference profiles are plotted in green dashed line and the reconstruction profiles in red.

the same processing for non-truncated projections). Similarly, the reconstructions of the fan-beam FBP are the same in configurations 1 and 2.

For configuration 3, the ROI is restricted to the part of the object inside the convex hull of the virtual trajectory. For FBP, we can only distinguish the high-contrast structures, whereas the five VFB formulas provide accurate reconstruction in the ROI. Compared to configuration 2, the streaks observed in the reconstructions of (a), (b) and (c) are different and less numerous. The profiles along the white horizontal line show that the artefacts are not symmetric and differ for each formula. Images reconstructed from simulations of the same head phantom without the right inner ear (not shown) do not display such an asymmetry, which suggests that the asymmetry stems from streaks produced by the density features of the right inner ear. For (c), a black and white pattern can now be observed close to the virtual trajectory boundaries. For (d), streak artefacts at the edges of interfaces between areas with different densities are now visible, with some common to (b), (c) and (d), and others observed for (d) only. For (e), no streak artefacts are observed but some stripe artefacts absent in configurations 1 and 2 appear now in configuration 3 at the left of the left eye and the right of the right eye (they can be seen on the left and right extremities of the profile of formula (e) in figure 9)).

For the thorax phantom (configuration 4), the ROI is also restricted to the part of the object inside the convex hull of the virtual trajectory. Again, the FBP reconstruction is very poor, whereas the five VFB formulas provide excellent reconstruction inside the ROI. The profiles along the white horizontal line show that the VFB reconstructions are similar on the right side but not on the left side, where (a) and (e) have the lowest artefacts and (c) the largest.

For the four configurations studied, we computed the normalised mean absolute errors (nMAE) in the ROI where exact reconstruction is expected of the VFB formulas between the reconstructed images and the reference images, and display them in table 2.

Table 2. Normalised mean absolute error (nMAE) between the reconstructed images and the reference images (see figure 7 left), restricted to the ROI where exact reconstruction is performed by the VFB formulas (see figures 5 and 6), for the four configurations studied, with noise-free data, and multiplied by a factor 10^3.

configuration	1	2	3	4
FBP	16.3	16.3	131.9	313.2
(a)	18.8	20.0	24.8	12.9
(b)	18.8	20.4	23.4	14.7
(c)	17.4	20.0	24.3	14.0
(d)	17.2	17.2	23.2	13.6
(e)	17.2	17.2	23.2	11.5

We observe that the FBP values are slightly smaller than the VFB values when

there is no truncation (configurations 1 and 2), but much higher in the presence of truncation (configurations 3 and 4). Among the five VFB formulas, there are minor differences, with the smallest values obtained by (d) and (e) for configurations 1, 2 and 3, and by (e) for configuration 4.

We now perform an analysis of spatial resolution on the reconstructions of the head phantom (configurations 1, 2 and 3). We select an elliptical interface of the head phantom (drawn in red in figure 7 left) for which we can approximate the radial edge-spread function (ESF) as

$$\mathrm{ESF}(x) = A\left(1 + \mathrm{erf}\left(\frac{x-1}{\sqrt{2}b}\right)\right) + c \tag{61}$$

where x represents the distance to the edge (such that $x = 0$ at the center of the interface and $x = 1$ at the border of the interface in figure 7 left), and erf is the Gauss error function. Then, following (Richard et al. 2012), the modulation transfer function (MTF) derived from this ESF is

$$\mathrm{MTF}(\xi) = e^{-2\pi^2 b^2 \xi^2} \tag{62}$$

and the frequency at which the MTF is 10 % of the maximum is

$$\xi_{10\%} = \sqrt{\frac{\ln 10}{2}}\frac{1}{\pi b}. \tag{63}$$

Finally, the uncertainty associated with the $\xi_{10\%}$ estimate is

$$\sigma = \sqrt{\frac{\ln 10}{2}}\frac{1}{\pi b^2}\sigma_{\mathrm{ESF}} \tag{64}$$

with σ_{ESF} the standard deviation error of the fitted parameter b of the ESF (61) (provided by the fitting routine curve_fit of the software package SciPy). For configurations 1, 2 and 3, we display in table 3 the frequency $\xi_{10\%} \pm 3\sigma$ (the interval $[\xi_{10\%} - 3\sigma, \xi_{10\%} + 3\sigma]$ has a probability of 99.7% to contain $\xi_{10\%}$ assuming a normal distribution of the error) for the elliptic interface of the head phantom drawn in red in figure 7 left.

Table 3. Quantitative assessment of the spatial resolution with the 10 % MTF frequency $\xi_{10\%} \pm 3\sigma$ measured at an elliptic interface of the head phantom (see figure 7 left).

configuration	1	2	3
FBP	36.9 ± 2.0	36.9 ± 2.0	36.1 ± 3.4
(a)	20.6 ± 0.6	18.7 ± 0.6	21.1 ± 0.8
(b)	20.9 ± 0.6	17.2 ± 0.7	24.0 ± 0.8
(c)	23.0 ± 0.7	19.2 ± 0.9	27.0 ± 1.0
(d)	23.6 ± 0.7	23.6 ± 0.7	24.6 ± 0.7
(e)	23.6 ± 0.7	23.6 ± 0.7	23.9 ± 0.7

We observe that the FBP values are higher than the VFB values in all cases, and configuration 3 suffers from a higher fitting error due to the image artefacts seen in

figure 9. For the VFB formulas, the MTF values are the highest for configuration 3 and the lowest for configuration 2, with configuration 1 in between. Among those five formulas, the spatial resolution differs marginally, with the best results obtained by (c) for configuration 3, and (d) and (e) for configurations 1 and 2.

4.2.2. Noisy projections

We also analyzed the robustness of the reconstructions with respect to noise for the truncated configuration 3. We assume that the detector individually counts the photons and that this counting is modeled by a Poisson law applied to the emerging photons beam $I_1 = I_0 \exp(-\int_L \mu \mathrm{d}l)$ where we take for initial beam $I_0 = 10^7$ photons. Because the values of the phantoms represent the density ρ (in g.cm^{-3}) and not the linear attenuation coefficient μ (in cm^{-1}), we multiply the sinogram by the mass attenuation coefficient of water at 75 keV, $\tau_{H_2O} = 0.1879$ cm^{2}g^{-1}, to obtain line-integrals of μ.

For a single simulation with noisy data, we compute the nMAE between the reconstructed images and the reference images, as we did in the noise-free case, and display it in table 4. Similar to the noise-free case, the FBP values are smaller than the

Table 4. Normalised mean absolute error (nMAE) between the reconstructed images and the reference images (see figure 7 left), restricted to the ROI where exact reconstruction is performed by the VFB formulas (see figures 5 and 6), for the four configurations studied, with noisy data.

configuration	1	2	3	4
FBP	17.1	17.1	131.9	313.2
(a)	19.2	20.4	25.2	15.6
(b)	19.2	20.7	23.9	17.4
(c)	17.8	20.3	24.9	16.8
(d)	17.7	17.7	23.8	18.5
(e)	17.7	17.7	23.8	16.2

VFB values in the absence of truncation and much higher in the presence of truncation. Among the VFB values, the smallest values are again obtained by (d) and (e) in configurations 1, 2 and 3, but in configuration 4, it is now (a) which has the lowest value.

Then, for each formula, we perform 100 simulations with a different noise realization and we compute the point-wise variance between the 100 reconstructions. Figure 11 shows the images of the variance in each pixel for configuration 3.

We observe that, for the FBP, the variance is much higher than for the five VFB formulas (the plotting scale used for FBP is 2.5 times bigger than the scale used for the VFB formulas). For formula (c), the variance is the highest around the virtual trajectory. Among the other four VFB formulas, which are all rather close, (a) shows the lowest variance, followed by (b) and (d), and then (e).

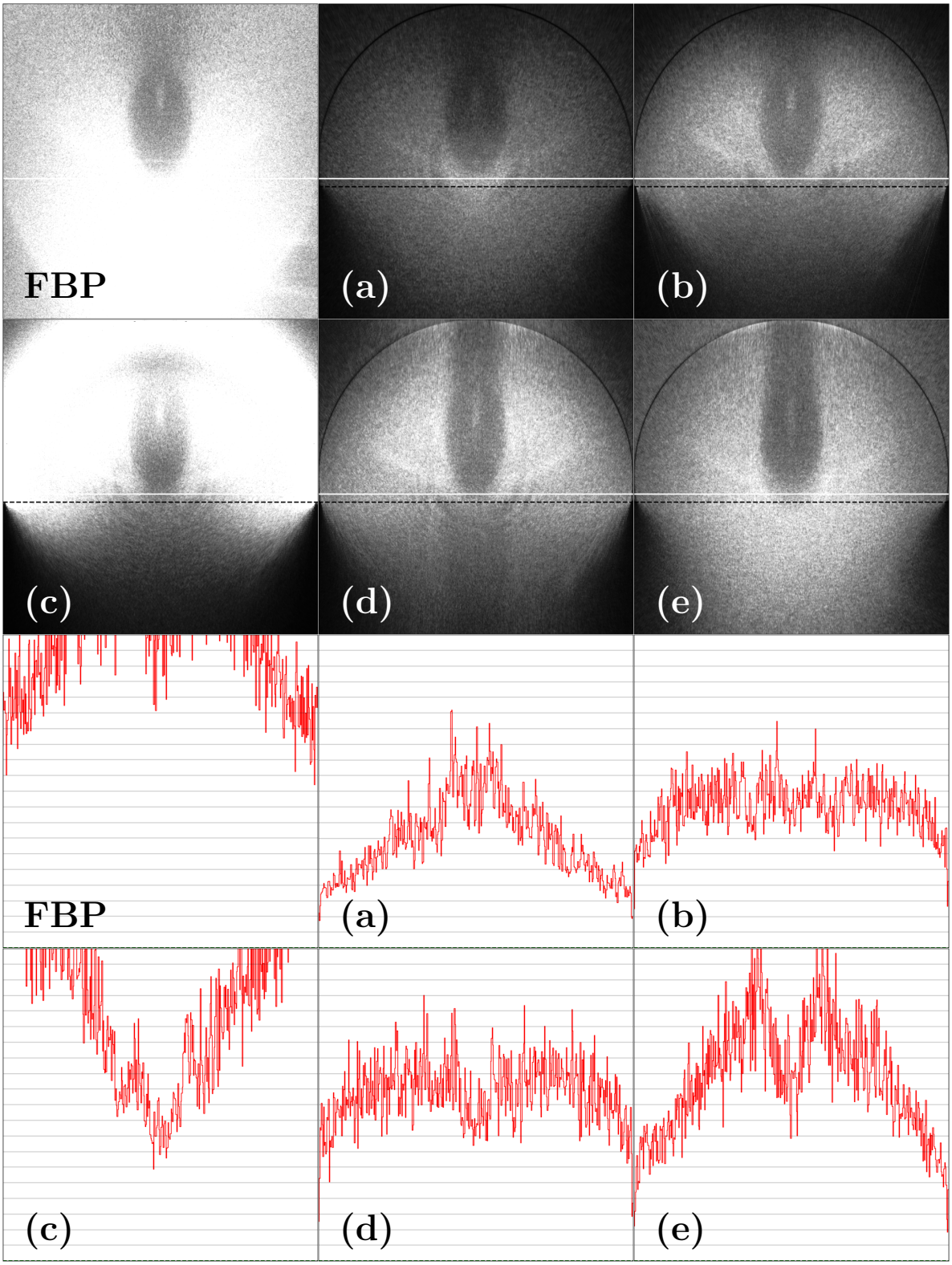

Figure 11. Top rows: variance of 100 image reconstructions from noisy projections of the head phantom with $R_V = 9$ cm (configuration 3) for the fan-beam FBP and the five VFB formulas. The horizontal black dashed line defines the boundary of the possible reconstruction area. The plotting scale is [0 (black), 10^{-5} (white)] for the VFB formulas and [0 (black), $2.5 \cdot 10^{-5}$ (white)] for the fan-beam FBP . Bottom rows: variance profiles corresponding to the white horizontal line, plotted with scale [0, 10^{-5}] for the VFB formulas and scale [0, $2.5 \cdot 10^{-5}$] for the fan-beam FBP.

5. Discussion

We have presented five VFB formulas, two of which, (d) and (e), are, to the best of our knowledge, new. Their novelty is that they perform the backprojection in the fan-beam acquisition geometry, and thus avoid rebinning steps for the non-truncated acquisition projections. In the literature, previous VFB formulas were either specific to parallel data (Clackdoyle & Noo 2004, Clackdoyle et al. 2006, Ould-Mohamed et al. 2007) or performed the backprojection in the parallel geometry after an explicit rebinning from the virtual geometry (Clackdoyle et al. 2004). The difference between (d) and (e) is that formula (d) uses explicit rebinning steps between the acquisition geometry and the virtual geometry, whereas formula (e) directly processes the truncated projections in the acquisition geometry (similarly to the formulas of Clackdoyle et al. (2006) and Ould-Mohamed et al. (2007) which directly process truncated parallel projections).

We compared our two new VFB formulas to fan-beam FBP and to three already known VFB formulas, called (a), (b) and (c), which perform the backprojection either in parallel, for (a) and (b), or in the virtual fan-beam geometry, for (c). The computation time of the VFB formulas in configuration 3 was approximately 16 sec for (a) and (b), 38 sec for (c), 74 sec for (d) and 98 sec for (e), for a non-optimised implementation (using a hand-made 2d interpolation, and with a pre-computation of the redundancy weight in (c), (d), (e) for each backprojection ray before the backprojection, to make faster the parallelized computation of the 100 simulations for the variance). As mentioned in the computational complexity analysis of section 3.5, parallel backprojection is faster than fan-beam backprojection since it does not have to compute the backprojection weight $1/||\vec{x} - R_V\vec{\theta}_\lambda||$, which explains why formulas (a) and (b) require less computation time. Regarding the formulas with fan-beam backprojection, (c) is computationally faster than (d) since it has one rebinning step fewer (for the truncated projections, which represent the majority of projections in configuration 3) and performs backprojection over a shorter scan. Formula (e) is slower than (d) as its filtering step is not a convolution, and so cannot be implemented using the fast Fourier transform. If the calculation time is an issue for a particular application, then it is preferable to use formula (a), (b) or (c), which produces comparable image quality to (d) and (e) for a factor five less in computation time.

We performed numerical experiments in four configurations (two without truncation and two with truncation), using two Forbild phantoms (head and thorax). We used a discontinuous redundancy weight w^{R_V}, defined in equation (33), and no noticeable difference was observed compared to the results (not shown) obtained using a smooth weight as the one defined by Noo et al. (2002).

The numerical results have shown that all formulas obtain satisfactory results for the non-truncated configurations 1 and 2, with noticeably more streaks in configuration 2 for formulas (a), (b) especially, and (c). Additional simulations (not displayed) showed that the streak sizes increase as R_V decreases between 45 and 13 cm, and also that the streaks are smaller if the virtual projections are directly computed with RTK instead of

being interpolated from acquisition projections with (36). So, we deduce that the streaks are caused by interpolating between two fan-beam geometries with very different radii. This applies not only to (36), but also (40) and (42), since the parallel geometry can be considered as a fan-beam geometry of infinite radius. In configuration 1, $R_V = R_A$ so (36) generates no interpolation errors, and R_V is large enough for the virtual projections to be almost parallel as they pass through the object, so (40) and (42) generate very small interpolation errors. In configuration 2, R_V is much smaller than R_A, so (36) now generates significant interpolation errors, and the same applies to (40) and (42), since R_V is much smaller than infinity. This explanation is consistent with the smaller streaks observed in (c), compared to (b), since (c) avoids the rebinning step (42). Smaller streaks are also observed in (a), compared to (b), which suggests that (42) generates more interpolation errors than (40). This difference can be explained by the differentiation step present in $g_F^{R_V}$, but not in $g_H^{R_V}$, which makes the values of $g_F^{R_V}$ higher than those of $g_H^{R_V}$ at interfaces, and therefore leads to more errors when interpolating values from $g_F^{R_V}$ instead of $g_H^{R_V}$. The ring of white artefacts observed around the virtual trajectory and the black and white pattern in formula (c) reconstruction of configuration 2 seem to be caused by the backprojection step when the trajectory of radius R_V is very close to the object, since the weight $1/||\vec{x} - R_V\vec{\theta}_\lambda||$ increases when $||\vec{x}||$ gets closer to R_V.

For the truncated configurations 3 and 4, the fan-beam FBP reconstructions suffer from dramatic artefacts, whereas the VFB formulas give good reconstructions in the convex hull of the virtual trajectory, as expected. Surprisingly, for formulas (a) and (b), there are fewer streaks observed in configuration 3 than in configuration 2, although we use an even smaller virtual radius than in configuration 2. Reconstructions of the head phantom without the right inner ear (not displayed) showed that most of the streaks observed for (a) and (b) in configuration 2 are due to the density features of the right inner ear. Looking at the streaks above the right eye in the reconstruction of formula (b) in configuration 2, we see that the lines along those streaks intersect the virtual trajectory at two points in configuration 2 and at a single point in configuration 3. Of those three intersections, the closest to the right inner ear - likely to be the most affected by the density features of the right inner ear - is one of the two intersection from configuration 2, which could explain why these streaks are observed in configuration 2 but not in configuration 3. For formula (d), some of the streak artefacts appearing in configuration 3 can also be observed with formulas (b) and (c), so they seem to be due to the combination of the interpolation step (36) and the differentiation step in the virtual geometry, which are common only to (b), (c) and (d). For formula (e), the absence of many streaks observed with (d) in configurations 3 and 4 may be explained by the reduced number of interpolations performed by (e), compared to (d). On the other hand, the stripe artefacts appearing in configuration 3 for formula (e) could be caused by an edge effect of the filtering procedure of (53): when formula (e) is discretized, the contributions of the rays of angles $-\gamma_m$ and γ_m in the integral of equation (53) cancel each other, so the angular intervals $(-\gamma_m, -\gamma_m + \Delta_\gamma)$ and $(\gamma_m - \Delta_\gamma, \gamma_m)$ are not taken into account. This data discarding may seem minor since it concerns only a $2\Delta_\gamma$ angular

interval in the acquisition geometry. However, the corresponding angular interval in the virtual geometry is much larger (as pointed out in section 3.1), so from the virtual geometry viewpoint, this data discarding is substantial and it may explain the artefacts observed.

The computation of nMAE between the reconstructed and reference images in the ROI shows that in absence of truncation (configurations 1 and 2), the best reconstruction is obtained by the FBP, followed by (d) and (e), and that in presence of truncation (configurations 3 and 4), the best result is produced by formula (e). In configurations 1 and 2, there is no truncation so formulas (d) and (e) correspond both to the SSS formula (32) applied to a full circular trajectory. Therefore, unlike formulas (a), (b) and (c), they do not perform interpolations to obtain the filtered acquisition projections, which may explain their superiority over (a), (b) and (c). Regarding the superiority of the FBP over (d) and (e), we conjecture that the discretization of the ramp filtering step in (60) leads to fewer numerical errors than discretizing the differentiation and Hilbert filtering steps in (11). In case of truncation, the FBP values are much higher, while the VFB values are similar to those computed without truncation. This confirms that the VFB formulas can reconstruct accurately a ROI in presence of truncation, unlike FBP. Among the VFB formulas, formula (e) performs fewer interpolations than the others, which means fewer numerical errors and explains why this formula obtains the smallest nMAE.

The quantification of the spatial resolution with the MTF analysis shows that fan-beam FBP outperforms all five VFB formulas. This could be explained by the differentiation step, present in all VFB formulas but not in FBP, which uses data from neighbouring pixels when discretized and is likely to cause a loss of resolution. The VFB results are quite similar, with (c) slightly better in configuration 3. The differences may be explained by the required number of interpolation steps. In configuration 1, the fan-beam acquisition and virtual geometries are the same, so only formulas (a) and (b) perform an interpolation (with equations (40) and (42)), and this can explain why they obtain the lowest MTF. In configuration 2, the virtual geometry has a different radius than the acquisition geometry so all the VFB formulas but (d) and (e) perform additional interpolations, and it may explain the decrease of spatial resolution between configurations 1 and 2 for formulas (a), (b), (c). Among the five VFB formulas, (c) performs one less interpolation than (a) and (b) since its backprojection is performed in the virtual geometry, while (d) and (e) perform no interpolation since the data are not truncated so it can explain why formulas (d) and (e) have the best spatial resolution, followed by formula (c). In configuration 3, the MTF results are surprising as they are even better than in configuration 1 for all five VFB formulas, despite the fact that formulas (d) and (e) perform some interpolation. The least interpolations is performed by (e) (only 1D interpolations on the first variable in (53)), followed by (c), and then by (a), (b) and (d). The fact that (e) did not have the best MTF may be explained by the edge effect presented above. The improvement of spatial resolution for all five VFB formulas in configuration 3, compared to configurations 1 and 2, could be explained

by the fact that with a trajectory which is not a full circle, filtered contributions from opposite source positions are less often averaged, the averaging of data being a source of spatial resolution loss.

Regarding the robustness to noisy data, the variance study shows that the results are, as expected, quite opposite to those of spatial resolution. The more robust formula to noise is (a), followed by (b) and (d), then (e), next (c), and finally FBP, which is the most affected by noise. More interpolations (for formulas (a), (b) and (d), compared to formulas (c), (e) and FBP) means more averaging, so less noise and a lowest variance but also a worse spatial resolution. For formula (c), the very high variance around the virtual trajectory seems to be caused by the backprojection weight $1/||\vec{x} - R_V\vec{\theta}_\lambda||$. For FBP, the very high variance observed (we recall that the plotting scale is 2.5 times bigger than for the other formulas) suggests that the filtering of truncated projections is very sensitive to noise.

One interesting feature of formulas (d) and (e) is that, in the absence of truncation, they simplify to FBP formulas. Moreover, the innovation of performing the backprojection in the acquisition geometry may pave the way for an extension of the VFB method to 3D approximate reconstruction from transversely-truncated cone-beam projections acquired with a full circular scan, where the well-known FDK (Feldkamp et al. 1984) algorithm produces severe truncation artefacts. A first extension has been reported by Charles et al. (2022).

6. Conclusion

In this paper, we have presented full mathematical derivations for five VFB formulas, two with a parallel backprojection and three with a fan-beam backprojection, one being performed in the virtual geometry and two in the acquisition geometry. We believe the latter two formulas, which do a fan-beam backprojection in the acquisition geometry, to be new. The numerical simulations indicate that the two new VFB formulas yield reconstructed images with a spatial resolution and a robustness to noise comparable to the three previously known VFB formulas.

Appendix A.

In this section, we rewrite

$$f_1(\vec{x}) = \int_0^\pi \left[w^R(\lambda_1, \gamma_1) \left(\frac{-1}{\sqrt{R^2 - s^2}} \right) g_F^R(\lambda_1, \gamma_1) \right] \Big|_{s=\vec{x}\cdot\vec{\eta}_\phi} \mathrm{d}\phi \tag{A.1}$$

and

$$f_2(\vec{x}) = \int_0^\pi \left[w^R(\lambda_2, \gamma_2) \left(\frac{-1}{\sqrt{R^2 - s^2}} \right) g_F^R(\lambda_2, \gamma_2) \right] \Big|_{s=\vec{x}\cdot\vec{\eta}_\phi} \mathrm{d}\phi \tag{A.2}$$

to obtain (26) and (27).

Starting with $f_1(\vec{x})$, we perform a change of variables $\phi \to \bar{\lambda}$ defined by $\bar{\lambda} = \lambda_1(\phi, s)|_{s=\vec{x}\cdot\vec{\eta}_\phi} = \phi + \pi - \arcsin(\vec{x} \cdot \vec{\eta}_\phi / R)$. To verify that this change of variables

is valid, we note that $\partial\bar{\lambda}/\partial\phi = 1 + \vec{x}\cdot\vec{\theta}_\phi/\sqrt{R^2-(\vec{x}\cdot\vec{\eta}_\phi)^2}$ which is strictly positive and therefore $\bar{\lambda}$ is a monotone function of ϕ. (Note that $||\vec{x}|| < R$ implies that $R^2 > ||\vec{x}||^2 = (\vec{x}\cdot\vec{\theta}_\phi)^2 + (\vec{x}\cdot\vec{\eta}_\phi)^2$, so $|\vec{x}\cdot\vec{\theta}_\phi|/\sqrt{R^2-(\vec{x}\cdot\vec{\eta}_\phi)^2} < 1$ from which $\partial\bar{\lambda}/\partial\phi > 0$.) Therefore we can write

$$f_1(\vec{x}) = \int_{\Lambda_1(\vec{x})} \left[w^R(\bar{\lambda},\gamma) g_F^R(\bar{\lambda},\gamma)\right]\big|_{\gamma=\bar{\gamma}_{\vec{x},\bar{\lambda}}} \frac{-1}{\sqrt{R^2-(\vec{x}\cdot\vec{\eta}_\phi)^2}} |\overline{J}| \mathrm{d}\bar{\lambda}. \tag{A.3}$$

Here $\Lambda_1(\vec{x})$ is the $\bar{\lambda}$ interval corresponding to $\phi \in [0,\pi)$, so $\Lambda_1(\vec{x}) = [\pi - \arcsin(x_2/R), 2\pi + \arcsin(x_2/R))$ where $\vec{x} = (x_1, x_2)$. The Jacobian $\overline{J}$ is $1/(\partial\bar{\lambda}/\partial\phi)$, and the product $\overline{J}/\sqrt{R^2-(\vec{x}\cdot\vec{\eta}_\phi)^2}$ turns out to be $1/||\vec{x}-R\vec{\theta}_{\bar{\lambda}}||$ as we show below. The expression for $\bar{\gamma}_{\vec{x},\bar{\lambda}}$ also depends on both $\vec{x}$ and $\bar{\lambda}$, and will be given explicitly below; it corresponds geometrically to the "γ-value" of the ray from the source at location $\bar{\lambda}$ passing through the point $\vec{x}$. We first evaluate the expression $||\vec{x}-R\vec{\theta}_{\bar{\lambda}}||^2$, using the identities $\vec{\theta}_A\cdot\vec{\theta}_B = \cos(A-B)$ and $\vec{\theta}_A\cdot\vec{\eta}_B = \sin(A-B)$.

$$\begin{aligned}
||\vec{x}-R\vec{\theta}_{\bar{\lambda}}||^2 &= [(\vec{x}-R\vec{\theta}_{\bar{\lambda}})\cdot\vec{\theta}_\phi]^2 + [(\vec{x}-R\vec{\theta}_{\bar{\lambda}})\cdot\vec{\eta}_\phi]^2 \\
&= (\vec{x}\cdot\vec{\theta}_\phi - R\cos(\bar{\lambda}-\phi))^2 + (\vec{x}\cdot\vec{\eta}_\phi - R\sin(\bar{\lambda}-\phi))^2 \\
&= \left(\vec{x}\cdot\vec{\theta}_\phi + R\sqrt{1-(\vec{x}\cdot\vec{\eta}_\phi/R)^2}\right)^2 + (\vec{x}\cdot\vec{\eta}_\phi - R(\vec{x}\cdot\vec{\eta}_\phi/R))^2 \\
&= \left(\vec{x}\cdot\vec{\theta}_\phi + \sqrt{R^2-(\vec{x}\cdot\vec{\eta}_\phi)^2}\right)^2
\end{aligned} \tag{A.4}$$

where the third line arises from applying the definition of $\bar{\lambda}$ as follows:

$$\cos(\bar{\lambda}-\phi) = \cos(\pi - \arcsin(\vec{x}\cdot\vec{\eta}_\phi/R)) = -\sqrt{1-(\vec{x}\cdot\vec{\eta}_\phi/R)^2}, \tag{A.5}$$

$$\sin(\bar{\lambda}-\phi) = \sin(\pi - \arcsin(\vec{x}\cdot\vec{\eta}_\phi/R)) = \vec{x}\cdot\vec{\eta}_\phi/R. \tag{A.6}$$

Now, from (A.4), we can compute $|\overline{J}|/\sqrt{R^2-(\vec{x}\cdot\vec{\eta}_\phi)^2}$.

$$\begin{aligned}
\frac{|\overline{J}|}{\sqrt{R^2-(\vec{x}\cdot\vec{\eta}_\phi)^2}} &= \frac{1}{|\partial\bar{\lambda}/\partial\phi|}\frac{1}{\sqrt{R^2-(\vec{x}\cdot\vec{\eta}_\phi)^2}} \\
&= \frac{1}{|1+\vec{x}\cdot\vec{\theta}_\phi/\sqrt{R^2-(\vec{x}\cdot\vec{\eta}_\phi)^2}|}\frac{1}{\sqrt{R^2-(\vec{x}\cdot\vec{\eta}_\phi)^2}} \\
&= \frac{1}{|\sqrt{R^2-(\vec{x}\cdot\vec{\eta}_\phi)^2}+\vec{x}\cdot\vec{\theta}_\phi|} = \frac{1}{||\vec{x}-R\vec{\theta}_{\bar{\lambda}}||}
\end{aligned} \tag{A.7}$$

so, from (A.7) and (A.3), we obtain

$$f_1(\vec{x}) = -\int_{\Lambda_1(\vec{x})} \frac{1}{||\vec{x}-R\vec{\theta}_{\bar{\lambda}}||}\left[w^R(\bar{\lambda},\gamma) g_F^R(\bar{\lambda},\gamma)\right]\big|_{\gamma=\bar{\gamma}_{\vec{x},\bar{\lambda}}} \mathrm{d}\bar{\lambda}. \tag{A.8}$$

We now examine $\bar{\gamma}_{\vec{x},\bar{\lambda}}$ which arises from $\gamma_1|_{s=\vec{x}\cdot\vec{\eta}_\phi}$ followed by the change of variables from ϕ to $\bar{\lambda}$. In terms of ϕ, we have $\bar{\gamma}_{\vec{x},\bar{\lambda}} = \arcsin(\vec{x}\cdot\vec{\eta}_\phi/R)$. We show below that

$$\bar{\gamma}_{\vec{x},\bar{\lambda}} = -\arcsin\left(\frac{\vec{x}\cdot\vec{\eta}_{\bar{\lambda}}}{||\vec{x}-R\vec{\theta}_{\bar{\lambda}}||}\right). \tag{A.9}$$

We have already seen that $||\vec{x}|| < R$ implies $\vec{x}\cdot\vec{\theta}_\phi + \sqrt{R^2-(\vec{x}\cdot\vec{\eta}_\phi)^2} > 0$. From this and (A.4), we obtain $||\vec{x}-R\vec{\theta}_{\bar{\lambda}}|| = \vec{x}\cdot\vec{\theta}_\phi + \sqrt{R^2-(\vec{x}\cdot\vec{\eta}_\phi)^2}$, which, combined with the identities $\cos\arcsin s = \sqrt{1-s^2}$, $\vec{\theta}_A\cdot\vec{\theta}_B = \cos(A-B)$, $\vec{\theta}_A\cdot\vec{\eta}_B = \sin(A-B)$, yields

$$\begin{aligned}
\frac{\vec{x}\cdot\vec{\eta}_\phi}{R} &= \frac{\vec{x}\cdot\vec{\eta}_\phi}{R}\ \frac{\vec{x}\cdot\vec{\theta}_\phi/R + \cos\arcsin(\vec{x}\cdot\vec{\eta}_\phi/R)}{\vec{x}\cdot\vec{\theta}_\phi/R + \sqrt{1-(\vec{x}\cdot\vec{\eta}_\phi/R)^2}} \\
&= \frac{\vec{x}\cdot\vec{\theta}_\phi\ \sin\arcsin(\vec{x}\cdot\vec{\eta}_\phi/R) + \vec{x}\cdot\vec{\eta}_\phi\cos\arcsin(\vec{x}\cdot\vec{\eta}_\phi/R)}{\vec{x}\cdot\vec{\theta}_\phi + \sqrt{R^2-(\vec{x}\cdot\vec{\eta}_\phi)^2}} \\
&= \frac{[(\vec{x}\cdot\vec{\theta}_\phi)\ \vec{\theta}_\phi + (\vec{x}\cdot\vec{\eta}_\phi)\ \vec{\eta}_\phi]\cdot\vec{\eta}_{\phi-\arcsin(\vec{x}\cdot\vec{\eta}_\phi/R)}}{||\vec{x}-R\vec{\theta}_{\bar{\lambda}}||} \\
&= \frac{\vec{x}\cdot\vec{\eta}_{\phi-\arcsin(\vec{x}\cdot\vec{\eta}_\phi/R)}}{||\vec{x}-R\vec{\theta}_{\bar{\lambda}}||} = \frac{-\vec{x}\cdot\vec{\eta}_{\phi+\pi-\arcsin(\vec{x}\cdot\vec{\eta}_\phi/R)}}{||\vec{x}-R\vec{\theta}_{\bar{\lambda}}||} = \frac{-\vec{x}\cdot\vec{\eta}_{\bar{\lambda}}}{||\vec{x}-R\vec{\theta}_{\bar{\lambda}}||}, \qquad \text{(A.10)}
\end{aligned}$$

which establishes (A.9) and demonstrates (26).

We now focus on the second term $f_2(\vec{x})$ of (25). In this case, we perform the change of variables $\phi \to \bar{\bar{\lambda}}$ given by $\bar{\bar{\lambda}} = \lambda_2(\phi,s)|_{s=\vec{x}\cdot\vec{\eta}_\phi} = \phi + \arcsin(\vec{x}\cdot\vec{\eta}_\phi/R)$, which is a valid substitution by the same argument as for $\bar{\lambda}$. This time we find that $||\vec{x}-R\vec{\theta}_{\bar{\bar{\lambda}}}|| = \left|\vec{x}\cdot\vec{\theta}_\phi - \sqrt{R^2-(\vec{x}\cdot\vec{\eta}_\phi)^2}\right|$, which leads again to $|\bar{\bar{J}}|/\sqrt{R^2-(\vec{x}\cdot\vec{\eta}_\phi)^2} = 1/||\vec{x}-R\vec{\theta}_{\bar{\bar{\lambda}}}||$ where $\bar{\bar{J}} = 1/(\partial\bar{\bar{\lambda}}/\partial\phi)$. We thus find that

$$f_2(\vec{x}) = -\int_{\Lambda_2(\vec{x})} \frac{1}{||\vec{x}-R\vec{\theta}_{\bar{\bar{\lambda}}}||}\left[w^R(\bar{\bar{\lambda}},\gamma)g_F^R(\bar{\bar{\lambda}},\gamma)\right]\Big|_{\gamma=\bar{\bar{\gamma}}_{\vec{x},\bar{\bar{\lambda}}}} \mathrm{d}\bar{\bar{\lambda}} \qquad \text{(A.11)}$$

where $\Lambda_2(\vec{x})$ is the $\bar{\bar{\lambda}}$ interval corresponding to $\phi\in[0,\pi)$, so $\Lambda_2(\vec{x}) = [\arcsin(x_2/R), \pi - \arcsin(x_2/R))$. For $\bar{\bar{\gamma}}_{\vec{x},\bar{\bar{\lambda}}}$, we have $\bar{\bar{\gamma}}_{\vec{x},\bar{\bar{\lambda}}} = -\arcsin(\vec{x}\cdot\vec{\eta}_\phi/R)$, and, as $||\vec{x}-R\vec{\theta}_{\bar{\bar{\lambda}}}|| = \left|\vec{x}\cdot\vec{\theta}_\phi - \sqrt{R^2-(\vec{x}\cdot\vec{\eta}_\phi)^2}\right| = \sqrt{R^2-(\vec{x}\cdot\vec{\eta}_\phi)^2} - \vec{x}\cdot\vec{\theta}_\phi$ since $||\vec{x}|| < R$, a similar direct calculation yields

$$\bar{\bar{\gamma}}_{\vec{x},\bar{\bar{\lambda}}} = -\arcsin\left(\frac{\vec{x}\cdot\vec{\eta}_{\bar{\bar{\lambda}}}}{||\vec{x}-R\vec{\theta}_{\bar{\bar{\lambda}}}||}\right), \qquad \text{(A.12)}$$

which demonstrates (27).

Appendix B.

In this section, we determine an expression of the offset angle s^R (the index R means that we assume a fan-beam circular source trajectory, centered at the origin O, of radius R) for any source point S outside an object of elliptic support and center C (see figure B1 for an illustration of this situation). We first study at which condition this angle can be zero. Then, we show that otherwise a valid value is given by the angle between the line tangent to the trajectory at S and the line tangent to the object at I, the intersection of the segment CS with the object elliptic boundary. Finally, we compute the expression of this angle.

Let $S = R\vec{\theta}_\lambda$ denote the source point of angle λ and H_k denote the half-plane corresponding to the set of rays $\{R\vec{\theta}_\lambda + t\vec{\theta}_{\lambda+\pi+\gamma}, t \geq 0\}$ such that γ belongs to $(-\pi/2 + k, \pi/2 + k)$. We have to determine a value of $s^R(\lambda)$ such that $H_{s^R(\lambda)}$ contains the object support.

Geometrically, H_0 is the half-plane separated by the tangent to the circle of radius R at the point S and containing this circle. So if the object support is confined inside this circle, then we can take $s^R(\lambda) = 0$. Else, it means that the tangent to the circle at S intersects the object.

Let $\vec{T}_{traj}$ denote a direction vector of the tangent to the circular trajectory at S. We can see in figure B1) that the portion of the object not covered by H_0 is the part of the object at the right of $\vec{T}_{traj}$. Let C denote the center of the elliptic object, I denote the intersection of the segment CS with the object boundary and $\vec{T}_{obj}$ denote a direction vector of the tangent to the object at I. We see that the half-plane left to $\vec{T}_{obj}$ contains the full object. If $s^R(\lambda)$ denotes the angle from $\vec{T}_{traj}$ to $\vec{T}_{obj}$, then $H_{s^R(\lambda)}$ is the half-plane delimited by the line parallel to $\vec{T}_{obj}$ and passing through S. This plane contains the full object too, so this choice of offset angle $s^R(\lambda)$ is valid.

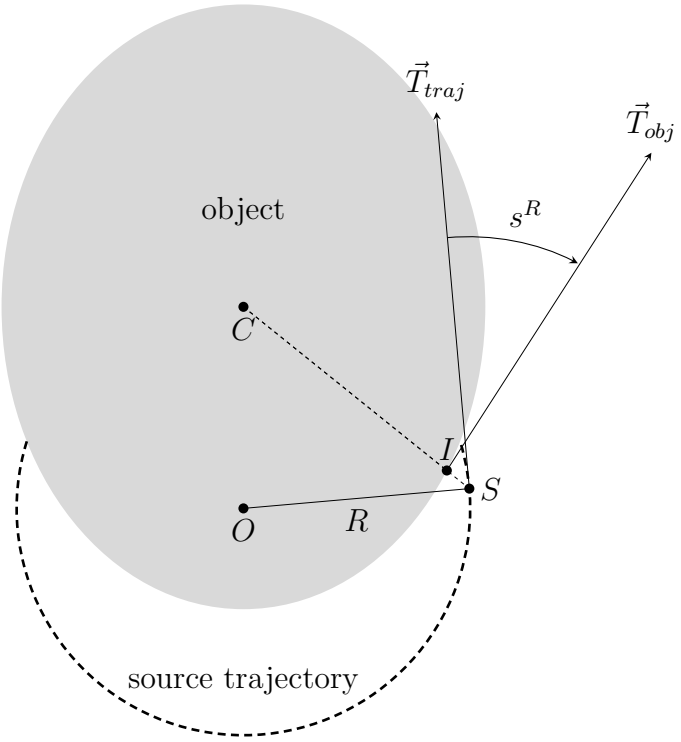

Figure B1. Determination of a valid offset angle s^R. I is the intersection of the segment CS with the object elliptic boundary. s^R is the angle between $\vec{T}_{traj}$, a direction vector of the tangent to the trajectory at S, and $\vec{T}_{obj}$, a direction vector of the tangent to the object at I. $\vec{T}_{obj}$ direction is chosen so that the half-plane to its left contains the object and $\vec{T}_{traj}$ direction is chosen so that the half-plane to its left contains the circular trajectory.

With this choice, for an object with elliptic support of center $C = (x_C, y_C)$, semi

major-axis a and semi-minor axis b, we have

$$s^R(\lambda) = \arctan\left(\frac{a^2\cos\lambda(R\sin\lambda - y_C) - b^2\sin\lambda(R\cos\lambda - x_C)}{a^2\sin\lambda(R\sin\lambda - y_C) + b^2\cos\lambda(R\cos\lambda - x_C)}\right) \tag{B.1}$$

To demonstrate this, we use the formula

$$\tan(s^R(\lambda)) = \frac{\det(\vec{T}_{traj}, \vec{T}_{obj})}{\vec{T}_{traj}\cdot\vec{T}_{obj}} \tag{B.2}$$

where $\det(\vec{u}(x,y), \vec{v}(x',y')) = xy' - x'y$. The equation of the tangent to the circle of center $O = (0,0)$ and radius R at $S = (x_S, y_S)$ is $x_S x + y_S y = R^2$. So a direction vector of this tangent is for instance $\vec{T}_{traj} = (-y_S, x_S) = (-R\sin\lambda, R\cos\lambda)$ (this choice is consistent with the direction of $\vec{T}_{traj}$ in figure B1). Similarly, the equation of the tangent to the ellipse of center $C = (x_C, y_C)$, semi major-axis a and semi-minor axis b at $I = (x_I, y_I)$ is

$$\frac{(x_I - x_C)(x - x_C)}{a^2} + \frac{(y_I - y_C)(y - y_C)}{b^2} = 1. \tag{B.3}$$

So a direction vector of this tangent is for instance $\vec{T}_{obj} = (-(y_I - y_C)/b^2, (x_I - x_C)/a^2)$ (this choice is consistent with the direction of $\vec{T}_{obj}$ in figure B1). Then, as $\overrightarrow{CI} = k\overrightarrow{CS}$ ($k \in (0,1)$), we have $(y_I - y_C)/k = (y_S - y_C)$ and $(x_I - x_C)/k = (x_S - x_C)$ so

$$\begin{aligned}\frac{1}{k}\vec{T}_{obj} &= \left(-\frac{y_S - y_C}{b^2}, \frac{x_S - x_C}{a^2}\right)\\ &= \left(-\frac{R\sin\lambda - y_C}{b^2}, \frac{R\cos\lambda - x_C}{a^2}\right)\end{aligned} \tag{B.4}$$

Since the norms of $\vec{T}_{traj}$ and $\vec{T}_{obj}$ play no role in the determination of $s^R(\lambda)$, we remove the factors R and k to simplify the following computations and use now

$$\left\{\begin{array}{rcl}\vec{T}_{traj} &=& (-\sin\lambda, \cos\lambda),\\ \vec{T}_{obj} &=& (-(R\sin\lambda - y_C)/b^2, (R\cos\lambda - x_C)/a^2).\end{array}\right. \tag{B.5}$$

It follows that

$$\begin{aligned}\det(\vec{T}_{traj}, \vec{T}_{obj}) &= -\sin\lambda\frac{R\cos\lambda - x_C}{a^2} + \cos\lambda\frac{R\sin\lambda - y_C}{b^2}\\ &= \frac{a^2\cos\lambda(R\sin\lambda - y_C) - b^2\sin\lambda(R\cos\lambda - x_C)}{a^2b^2}\end{aligned} \tag{B.6}$$

and

$$\begin{aligned}\vec{T}_{traj}\cdot\vec{T}_{obj} &= \frac{\sin\lambda(R\sin\lambda - y_C)}{b^2} + \frac{\cos\lambda(R\cos\lambda - x_C)}{a^2}\\ &= \frac{a^2\sin\lambda(R\sin\lambda - y_C) + b^2\cos\lambda(R\cos\lambda - x_C)}{a^2b^2}\end{aligned} \tag{B.7}$$

which, using equation (B.2), ends the demonstration.

Appendix C.

In this section, we demonstrate proposition 2. We first show how to express $g_F^{R_V}$ in terms of g^{R_A} by combining (11) and (36). Then, as $g_F^{R_A}$ is expressed in terms of $g_F^{R_V}$ in corollary (1), it will give an expression of $g_F^{R_A}$ in terms of g^{R_A}, as desired.

Starting from definition (11), we have

$$2\pi g_F^{R_V}(\lambda,\gamma_V) = \int_{-\pi}^{\pi} h_H(\sin(\gamma_V-\gamma))\left(\frac{\partial}{\partial\lambda}-\frac{\partial}{\partial\gamma}\right) g^{R_V}(\lambda,\gamma)\mathrm{d}\gamma. \tag{C.1}$$

For $\lambda \in \Lambda_{R_V}$, we know from (34) that $g^{R_V}(\lambda,\gamma_V)=0$ for $\gamma_V \in [-\pi,\pi)/\Gamma(s^{R_V}(\lambda))$, so the integral over $(-\pi,\pi)$ in (C.1) reduces to the integral over $\Gamma(s^{R_V}(\lambda)) = [-\pi/2 + s^{R_V}(\lambda), \pi/2 + s^{R_V}(\lambda))$. It follows that

$$2\pi g_F^{R_V}(\lambda,\gamma_V) = \int_{-\frac{\pi}{2}+s^{R_V}(\lambda)}^{\frac{\pi}{2}+s^{R_V}(\lambda)} h_H(\sin(\gamma_V-\gamma))\left(\frac{\partial}{\partial\lambda}-\frac{\partial}{\partial\gamma}\right) g^{R_V}(\lambda,\gamma)\mathrm{d}\gamma. \tag{C.2}$$

To perform a one-to-one change of variables between the virtual and acquisition settings, we need the integral in (C.2) to be over the interval $[-\pi/2,\pi/2)$ instead of $[-\pi/2 + s^{R_V}(\lambda), \pi/2 + s^{R_V}(\lambda))$. If $s^{R_V}(\lambda) \geq 0$, as $s^{R_V}(\lambda) \leq \pi$, we can write

$$\begin{aligned} 2\pi g_F^{R_V}(\lambda,\gamma_V) = &\int_{-\frac{\pi}{2}+s^{R_V}(\lambda)}^{\frac{\pi}{2}} h_H(\sin(\gamma_V-\gamma))\left(\frac{\partial}{\partial\lambda}-\frac{\partial}{\partial\gamma}\right) g^{R_V}(\lambda,\gamma)\mathrm{d}\gamma \\ &+ \int_{\frac{\pi}{2}}^{\frac{\pi}{2}+s^{R_V}(\lambda)} h_H(\sin(\gamma_V-\gamma))\left(\frac{\partial}{\partial\lambda}-\frac{\partial}{\partial\gamma}\right) g^{R_V}(\lambda,\gamma)\mathrm{d}\gamma \end{aligned} \tag{C.3}$$

where the second term (ST_{pos}) of (C.3), when translating γ by $-\pi$, can be expressed

$$\begin{aligned} ST_{\text{pos}} &= \int_{-\frac{\pi}{2}}^{-\frac{\pi}{2}+s^{R_V}(\lambda)} h_H(\sin(\gamma_V-(\gamma+\pi)))\left(\frac{\partial}{\partial\lambda}-\frac{\partial}{\partial\gamma}\right) g^{R_V}(\lambda,\gamma+\pi)\mathrm{d}\gamma \\ &= -\int_{-\frac{\pi}{2}}^{-\frac{\pi}{2}+s^{R_V}(\lambda)} h_H(\sin(\gamma_V-\gamma))\left(\frac{\partial}{\partial\lambda}-\frac{\partial}{\partial\gamma}\right) g^{R_V}(\lambda,\gamma)\mathrm{d}\gamma \end{aligned} \tag{C.4}$$

because $\sin(a-\pi) = -\sin a$, h_H is odd and $g^{R_V}(\lambda,\gamma+\pi) = g^{R_V}(\lambda,\gamma)$ when $\lambda \in \Lambda_{R_V}$. This last equality follows from (36):

$$\begin{aligned} g^{R_V}(\lambda,\gamma+\pi) &= p(\lambda+\gamma+\pi, -R_V\sin(\gamma+\pi)) \\ &= p(\lambda+\gamma+\pi, R_V\sin\gamma) \\ &= p(\lambda+\gamma, -R_V\sin\gamma) \text{ using (2)} \\ &= g^{R_V}(\lambda,\gamma). \end{aligned} \tag{C.5}$$

So, for $s^{R_V}(\lambda) \geq 0$, a minus sign appears for the interval $\gamma \in [-\pi/2, -\pi/2 + s^{R_V}(\lambda)]$.

When $s^{R_V}(\lambda) < 0$, as $s^{R_V}(\lambda) \geq -\pi$, a similar calculation shows that

$$\begin{aligned} 2\pi g_F^{R_V}(\lambda,\gamma) = &\int_{-\frac{\pi}{2}}^{\frac{\pi}{2}+s^{R_V}(\lambda)} h_H(\sin(\gamma_V-\gamma))\left(\frac{\partial}{\partial\lambda}-\frac{\partial}{\partial\gamma}\right) g^{R_V}(\lambda,\gamma)\mathrm{d}\gamma \\ &+ \int_{-\frac{\pi}{2}+s^{R_V}(\lambda)}^{-\frac{\pi}{2}} h_H(\sin(\gamma_V-\gamma))\left(\frac{\partial}{\partial\lambda}-\frac{\partial}{\partial\gamma}\right) g^{R_V}(\lambda,\gamma)\mathrm{d}\gamma \end{aligned} \tag{C.6}$$

where the second term (ST_{neg}) of (C.6), when translating γ by π, can be expressed

$$\begin{aligned} ST_{\text{neg}} &= \int_{\frac{\pi}{2}+s^{R_V}(\lambda)}^{\frac{\pi}{2}} h_H(\sin(\gamma_V-(\gamma-\pi)))\left(\frac{\partial}{\partial\lambda}-\frac{\partial}{\partial\gamma}\right)g^{R_V}(\lambda,\gamma-\pi)\mathrm{d}\gamma \\ &= -\int_{\frac{\pi}{2}+s^{R_V}(\lambda)}^{\frac{\pi}{2}} h_H(\sin(\gamma_V-\gamma))\left(\frac{\partial}{\partial\lambda}-\frac{\partial}{\partial\gamma}\right)g^{R_V}(\lambda,\gamma)\mathrm{d}\gamma. \end{aligned} \tag{C.7}$$

So, for $s^{R_V}(\lambda)\leq 0$, a minus sign appears for the interval $\gamma\in[\pi/2+s^{R_V}(\lambda),\pi/2]$.

In both cases, the minus appears for values of γ such that $|\gamma-s^{R_V}(\lambda)|>\pi/2$, so this minus can be expressed as $\text{sign}(\pi/2-|\gamma-s^{R_V}(\lambda)|)$ where $\text{sign}(u)=1$ if $u>0$, $\text{sign}(u)=-1$ if $u<0$, and $\text{sign}(0)=0$. Using this notation, the expression of the integrands of the first and second terms of both (C.4) and (C.6) become the same, and the integral ranges are contiguous with no overlap, so we obtain

$$\begin{aligned} g_F^{R_V}(\lambda,\gamma_V) = \frac{1}{2\pi}\int_{-\frac{\pi}{2}}^{\frac{\pi}{2}} & h_H(\sin(\gamma_V-\gamma))\ \text{sign}\left(\pi/2-\left|\gamma-s^{R_V}(\lambda)\right|\right) \\ & \left(\frac{\partial}{\partial\lambda}-\frac{\partial}{\partial\gamma}\right)g^{R_V}(\lambda,\gamma)\mathrm{d}\gamma. \end{aligned} \tag{C.8}$$

Now, from (36),

$$g^{R_V}(\lambda,\gamma)=\frac{1}{2}\left[g^{R_A}(\lambda+\gamma-\gamma_A^V,\gamma_A^V)+g^{R_A}(\lambda+\gamma+\pi+\gamma_A^V,-\gamma_A^V)\right] \tag{C.9}$$

so, as

$$\frac{\partial}{\partial\gamma}\gamma_A^V=\frac{\partial}{\partial\gamma}\arcsin\left(\frac{R_V}{R_A}\sin\gamma\right)=\frac{R_V\cos\gamma}{\sqrt{R_A^2-R_V^2\sin^2\gamma}}, \tag{C.10}$$

a short calculation shows that

$$\left(\frac{\partial}{\partial\lambda}-\frac{\partial}{\partial\gamma}\right)g^{R_V}(\lambda,\gamma)= \tag{C.11}$$

$$\frac{R_V\cos\gamma}{2\sqrt{R_A^2-R_V^2\sin^2\gamma}}\left[\partial g^{R_A}(\lambda+\gamma-\gamma_A^V,\gamma_A^V)-\partial g^{R_A}(\lambda+\gamma+\pi+\gamma_A^V,-\gamma_A^V)\right] \tag{C.12}$$

where

$$\partial g^{R_A}(\lambda,\gamma)=\left(\frac{\partial}{\partial\lambda}-\frac{\partial}{\partial\gamma}\right)g^{R_A}(\lambda,\gamma). \tag{C.13}$$

Using the change of variables $\gamma'=\gamma_A^V=\arcsin\left((R_V/R_A)\sin\gamma\right)$, with the Jacobian $|J|=1/|\mathrm{d}\gamma'/\mathrm{d}\gamma|=\sqrt{R_A^2-R_V^2\sin^2\gamma}/(R_V\cos\gamma)$ from (C.10), gives

$$\begin{aligned} g_F^{R_V}(\lambda,\gamma_V) = \frac{1}{4\pi}\int_{-\gamma_m}^{\gamma_m} & h_H\left(\sin\left(\gamma_V-\arcsin\left((R_A/R_V)\sin(\gamma')\right)\right)\right) \\ & \text{sign}\left(\pi/2-\left|\arcsin((R_A/R_V)\sin(\gamma'))-s^{R_V}(\lambda)\right|\right) \\ & \left[\partial g^{R_A}\left(\lambda+\arcsin\left((R_A/R_V)\sin(\gamma')\right)-\gamma',\gamma'\right)\right. \\ & \left.-\partial g^{R_A}\left(\lambda+\arcsin\left((R_A/R_V)\sin(\gamma')\right)+\pi+\gamma',-\gamma'\right)\right]\mathrm{d}\gamma'. \end{aligned} \tag{C.14}$$

We can finally use corollary 1:

$$g_F^{R_A}(\lambda,\gamma)=\frac{R_A\cos\gamma}{\sqrt{R_V^2-R_A^2\sin^2\gamma}}g_F^{R_V}(\lambda+\gamma-\gamma_V^A,\gamma_V^A). \tag{C.15}$$

Equation (C.14) is satisfied for all $\lambda \in \Lambda_{R_V}$. From the hypothesis of Proposition 2, we have $\lambda + \gamma - \gamma_V^A \in \Lambda_{R_V}$, so we can apply the result of (C.14) to the right hand side of (C.15) to obtain

$$\begin{aligned} g_F^{R_A}(\lambda,\gamma) = \frac{R_A \cos\gamma}{4\pi\sqrt{R_V^2 - R_A^2\sin^2\gamma}} \int_{-\gamma_m}^{\gamma_m} h_H\left(\sin\left(\gamma_V^A - {\gamma'}_V^A\right)\right) \\ \operatorname{sign}\left(\pi/2 - \left|{\gamma'}_V^A - s^{R_V}(\lambda+\gamma-\gamma_V^A)\right|\right) \\ \left[\partial g^{R_A}\left(\lambda+\gamma-\gamma_V^A+{\gamma'}_V^A-\gamma',\gamma'\right)\right. \\ \left.-\partial g^{R_A}\left(\lambda+\gamma-\gamma_V^A+{\gamma'}_V^A+\pi+\gamma',-\gamma'\right)\right]\mathrm{d}\gamma' \end{aligned} \tag{C.16}$$

which ends the demonstration of proposition 2.

Acknowledgment

The authors thank Dr. Feriel Khellaf for her help for the computation of the modulation transfer function. This work was partially supported by grants ANR-17-CE19-0006 (ROIdoré project) and ANR-21-CE45-0026 (SPECT-Motion-eDCC project) from the Agence Nationale de la Recherche, France.

Data availability statement

Any data that support the findings of this study are included within the article.

References

Charles, M., Clackdoyle, R. & Rit, S. (2021). Implementation of the virtual fan-beam method for 2D region-of-interest reconstruction from truncated data, *Fully 3D Image Reconstruction in Radiology and Nuclear Medicine*, Leuven, pp. 44–48.

Charles, M., Clackdoyle, R. & Rit, S. (2022). Cone-beam reconstruction for a circular trajectory with transversely-truncated projections based on the virtual fan-beam method, *in* J. W. Stayman (ed.), *7th International Conference on Image Formation in X-Ray Computed Tomography*, Vol. 12304, International Society for Optics and Photonics, SPIE, Baltimore, pp. 1230405–1 – 1230405–7.

Chen, G.-H. (2003). A new framework of image reconstruction from fan beam projections, *Medical Physics* **30**(6): 1151–1161.

Clackdoyle, R. & Defrise, M. (2010). Tomographic Reconstruction in the 21st Century, *IEEE Signal Processing Magazine* **27**(4): 60–80.

Clackdoyle, R. & Noo, F. (2004). A large class of inversion formulae for the 2D Radon transform of functions of compact support, *Inverse Problems* **20**(4): 1281–1291.

Clackdoyle, R., Noo, F., Guo, J. & Roberts, J. A. (2004). Quantitative reconstruction from truncated projections in classical tomography, *IEEE Transactions on Nuclear Science* **51**(5): 2570–2578.

Clackdoyle, R., Noo, F., Ould-Mohamed, M. S. & Mennessier, C. (2006). Filtered-Backprojection Reconstruction Formula for 2D Tomography with Bilateral Truncation, *2006 IEEE Nuclear Science Symposium Conference Record*, IEEE, San Diego, pp. 2895–2899.

Clackdoyle, R., Roy, D. N. G., Defrise, M., Mennessier, C. & Mohamed, M.-S. O. (2009). Two-dimensional region-of-interest reconstruction: Analyzing the difference between virtual fanbeam and DBP-Hilbert reconstructions, *2009 IEEE Nuclear Science Symposium Conference Record*, IEEE, Orlando, pp. 3367–3371.

Deans, S. R. (1983). *The Radon Transform and Some of Its Applications*, John Wiley & Sons.

Defrise, M., Noo, F., Clackdoyle, R. & Kudo, H. (2006). Truncated Hilbert transform and image reconstruction from limited tomographic data, *Inverse Problems* **22**(3): 1037–1053.

Feldkamp, L. A., Davis, L. C. & Kress, J. W. (1984). Practical cone-beam algorithm, *Journal of the Optical Society of America A* **1**(6): 612–919.

Fu, L., Liao, J. & Qi, J. (2006). Evaluation of 2D ROI Image Reconstruction Using ML-EM Method from Truncated Projections, *2006 IEEE Nuclear Science Symposium Conference Record*, IEEE, San Diego, pp. 2236–2241.

Guerrero, P., Bernardi, M. & Miqueles, E. (2023). Alternative fan-beam backprojection and adjoint operators, *Journal of Inverse and Ill-posed Problems* (to appear).

Hamaker, C., Smith, K. T., Solomon, D. C. & Wagner, S. L. (1980). The divergent beam x-ray transform, *Rocky Mountain Journal of Mathematics* **10**(1): 253–283.

Kak, A. C. & Slaney, M. (1988). *Principles of Computerized Tomographic Imaging*, IEEE Press.

Kudo, H., Noo, F., Defrise, M. & Clackdoyle, R. (2002). New super-short-scan algorithms for fan-beam and cone-beam reconstruction, *2002 IEEE Nuclear Science Symposium Conference Record*, IEEE, Norfolk, pp. 902–906.

Lauritsch, G. & Bruder, H. Head phantom, visited on 03/29/2023.
URL: *https://www.dkfz.de/en/roentgenbildgebung/ct/CT_Phantoms/Head_Phantom/Head_Phantom.html*

Lewitt, R. M. (1979). Processing of incomplete measurement data in computed tomography, *Medical Physics* **6**(5): 412–417.

Li, Y., Li, K., Zhang, C., Montoya, J. & G.-H.Chen (2019). Learning to Reconstruct Computed Tomography Images Directly From Sinogram Data Under A Variety of Data Acquisition Conditions, *IEEE Transactions on Medical Imaging* **38**(10): 2469–2481.

Louis, A. K. & Rieder, A. (1989). Incomplete data problems in X-ray computerized tomography, *Numerische Mathematik* **56**(4): 371–383.

Lux, P. (1981). Redundancy in 360° Direct Fan-Beam Reconstruction, *Mathematical Aspects of Computerized Tomography: Proceedings, Oberwolfach, February 10–16, 1980*, Springer Berlin Heidelberg, pp. 140–151.

Natterer, F. (1986). *The Mathematics of Computerized Tomography*, New-York: Wiley.

Noo, F., Clackdoyle, R. & Pack, J. D. (2004). A two-step Hilbert transform method for 2D image reconstruction, *Physics in Medicine and Biology* **49**(17): 3903–3923.

Noo, F., Defrise, M., Clackdoyle, R. & Kudo, H. (2002). Image reconstruction from fan-beam projections on less than a short scan, *Physics in Medicine and Biology* **47**(14): 2525–2546.

Ogawa, K., Nakajima, M. & Yuta, S. (1984). A Reconstruction Algorithm from Truncated Projections, *IEEE Transactions on Medical Imaging* **3**(1): 34–40.

Ohnesorge, B., Flohr, T., Schwarz, K., Heiken, J. P. & Bae, K. T. (2000). Efficient correction for CT image artifacts caused by objects extending outside the scan field of view, *Medical Physics* **27**(1): 39–46.

Ould-Mohamed, M. S., Clackdoyle, R. & Mennessier, C. (2008). Region-of-interest reconstruction from truncated data by combined classical filtered-backprojection and virtual fanbeam reconstruction, *2008 IEEE Nuclear Science Symposium Conference Record*, IEEE, Dresden, pp. 4178–4181.

Ould-Mohamed, M. S., Mennessier, C. & Clackdoyle, R. (2007). Even More Inversion Formulas for the 2D Radon Transform of Functions of Compact and Convex Support, *The 29th Annual*

International Conference of the IEEE Engineering in Medicine and Biology Society, pp. 4410–4413.

Rashed, E. A., Kudo, H. & Noo, F. (2009). Iterative Region-of-Interest Reconstruction From Truncated CT Projection Data Under Blind Object Support, *Medical Imaging Technology* **27**(5): 321–331.

Rashid-Farrokhi, F., Liu, K. J. R., Berenstein, C. A. & Walnut, D. (1997). Wavelet-based multiresolution local tomography, *IEEE Transactions on Image Processing* **6**(10): 1412–1430.

Richard, S., Husarik, D. B., Yadava, G., Murphy, S. N. & Samei, E. (2012). Towards task-based assessment of CT performance: System and object MTF across different reconstruction algorithms, *Medical Physics* **39**(7Part1): 4115–4122.

Rit, S., Oliva, M. V., Brousmiche, S., Labarbe, R., Sarrut, D. & Sharp, G. C. (2014). The Reconstruction Toolkit (RTK), an open-source cone-beam CT reconstruction toolkit based on the Insight Toolkit (ITK), *Journal of Physics: Conference Series* **489**: 012079–1 012079–4.

Sidky, E. Y., Kraemer, D. N., Roth, E. G., Ullberg, C., Reiser, I. S. & Pan, X. (2014). Analysis of iterative region-of-interest image reconstruction for x-ray computed tomography, *Journal of Medical Imaging* **1**(3): 031007–1 – 031007–16.

Sourbelle, K. Thorax phantom, visited on 03/29/2023.
URL: *https://www.dkfz.de/en/roentgenbildgebung/ct/CT_Phantoms/Thorax_Phantom/Thorax_Phantom.html*

Wolberg, G. (1990). *Digital image warping*, IEEE Computer Society Press, Los Alamitos, CA.

Zhang, B. & Zeng, G. L. (2007). Two-dimensional iterative region-of-interest (ROI) reconstruction from truncated projection data, *Medical Physics* **34**(3): 935–944.

Zhuang, T., Leng, S., Nett, B. E. & Chen, G. (2004). Fan-beam and cone-beam image reconstruction via filtering the backprojection image of differentiated projection data, *Physics in Medicine and Biology* **49**(24): 5489–5503.

Zou, Y., Pan, X. & Sidky, E. Y. (2004). Image reconstruction in regions-of-interest from truncated projections in a reduced fan-beam scan, *Physics in Medicine and Biology* **50**(1): 13–27.